TSUNAMI DEBRIS MOTION AND LOADS IN A SCALED PORT SETTING: COMPARATIVE ANALYSIS OF THREE STATE-OF-THE-ART NUMERICAL METHODS AGAINST EXPERIMENTS

Justin Bonus[1], Felix Spröer[2], Andrew Winter[3], Pedro Arduino[4], Clemens Krautwald[5], Michael Motley[6], and Nils Goseberg[7, 8]

[1]University of California, Berkeley. Dep. of Civil and Environmental Engineering
[1]Email: bonus@berkeley.edu
[3,4,6]University of Washington, Seattle. Dep. of Civil and Environmental Engineering
[3,4,6]Email: andrew25@uw.edu, parduino@uw.edu, mrmotley@uw.edu
[2,5,7]Technische Universität Braunschweig. Dept. of Hydromechanics, Coastal and Ocean Engineering
[2,5,7]Email: felix.sproeer@tu-braunschweig.de, c.krautwald@tu-braunschweig.de, n.goseberg@tu-braunschweig.de
[8]Coastal Research Center, Joint Research Facility of Leibniz Universität Hannover and Technische Universität Braunschweig, Hannover 30419, Germany
[8]Email: goseberg@fzk.uni-hannover.de

ABSTRACT

We present an international comparative analysis of simulated 3D tsunami debris hazards, applying three state-of-the-art numerical methods: the Material Point Method (MPM, ClaymoreUW, multi-GPU), Smoothed Particle Hydrodynamics (SPH, DualSPHysics, GPU), and Eulerian grid-based computational fluid dynamics (Simcenter STAR-CCM+, multi-CPU / GPU). Three teams, two from the United States and one from Germany, apply their unique expertise to shed light on the state of advanced tsunami debris modeling in both open source and professional software. A mutually accepted and meaningful benchmark is set as 1:40 Froude scale model experiments of shipping containers mobilized into and amidst a port setting with simplified and generic structures, closely related to the seminal Tohoku 2011 tsunami case histories which majorly affected seaports. A sophisticated wave flume at Waseda University in Tokyo, Japan, hosted the experiments as reported by Goseberg et al. 2016b. Across dozens of trials, an elongated vacuum-chamber wave surges and spills over a generic harbor apron, mobilizing 3–6 hollow debris -modeling sea containers-, in 1–2 vertical layers against friction. One to two rows of 5 square obstacles are placed upstream or downstream of the debris, with widths and gaps of 0.66x and 2.2x of debris length, respectively. The work reports and compares results on the long wave generation from a vacuum-controlled tsunami wave maker, longitudinal displacement of debris forward and back, lateral spreading angle of debris, interactions of stacked debris, and impact forces measured with debris accelerometers and/or obstacle load-cells. Each team writes a foreword on their digital twin model, which are all open-sourced. Then, preliminary statistical analysis contrasts simulations originating off different numerical methods, and simulations with experiments. Afterward, team's give value propositions for their numerical tool. Finally, a transparent cross-interrogation of results highlights the strengths of each respective method.

1 INTRODUCTION AND MOTIVATION

The threat to coastal communities arising from fast-onset flooding as a result of tsunami remains one of the most urgent natural hazard to plan for and to mitigate potential consequences. Flooding in the context

of built environments remains a challenge, given the multiple interactions between the flow, debris, and the structural inventory's configuration (Ayoub et al. 2022). Tsunami flooding threatens the life of coastal inhabitants, infrastructure, residential building stocks, and local port infrastructure and water resources; recent tsunami events have demonstrated destruction potential reaching multiple kilometers beyond the immediate coastal ports and communities. Compound hazards such as nuclear accidents, fire outbreaks, or release of toxic substances when tsunami hit port facilities have been observed and have given rise to current research (Ishiki et al. 2023; Hokugo et al. 2011). The understanding and replication of an extreme flow interaction with rigid building models or groups thereof has been attempted by various studies in the past years (Moon et al. 2020; Sogut et al. 2019; Bihs et al. 2017). High-velocity and debris-laden flows have shown a specifically destructive potential for residential buildings, which remains a major challenge for experimental and numerical modelling alike. Gautam et al. 2023 investigated the collapse potential of riparian reinforced concrete buildings exposed to river flooding, while Krautwald et al. 2022 demonstrated the challenges related to the experimental modelling of collapsible generic timber-frame constructions exposed to broken tsunami-like bores over horizontal flume bathymetries. These current works demonstrate the persistent lack of knowledge with respect to the interaction of extreme flow conditions and buildings (Goseberg et al. 2016a; Stolle et al. 2017a; Stolle et al. 2017b), and in this context it remains important to better understand the drivers for extreme loading on building members (Nistor et al. 2017a), often resulting from debris strikes advected within extreme flow conditions, or from overload as a result of debris damming (Stolle et al. 2020b).

This work hence presents a numerical comparative study of tsunami debris dynamics, in close collaboration between researchers in the United States and Germany. The primary, novel contribution is the critical examination of three numerical modeling methods for next-generation, high-performance tsunami debris motion, damming and loading simulations. Further, three digital twins of the pressurized tsunami wave flume at Waseda University, which uses vacuum-chambers to generate long waves, are created to replicate the tsunami debris wave flume experiments of Goseberg et al. 2016b. All implementations are high-performance computationally (multi-GPU/multi-CPU), with nearly identical settings synced across each. Using the Material Point Method in our open-source ClaymoreUW software, implemented in the HydroUQ application (McKenna et al. 2024), is the NHERI SimCenter (USA) team of Justin Bonus, Pedro Arduino, and Michael Motley. Smoothed Particle Hydrodynamics within the open-source DualSPHysics software is taken as the approach by Felix Spröer, Clemens Krautwald, and Nils Goseberg from the Technische Universität Braunschweig, Germany. Siemens STAR-CCM+ CFD is represented by Andrew Winter of Siemens and the University of Washington, USA.

This research provides insights into three state-of-the-art numerical approaches to high-fidelity tsunami debris modeling at a reduced physical scale. Results produced by the numerical approaches are affected by not only the software package version they are implemented in, but also a modeling team's application.

The Material Point Method (MPM)

The principal aim of this research is not only to evaluate the efficacy, precision, and reliability of these numerical techniques in modelling complex debris-fluid-structure interactions, but also to discern the degree to which obstacles affect the maximum longitudinal displacement and spreading angle of debris in the context of hazards posed to the built environment during natural disasters. The outcome of this research promises to yield insights that will guide the selection of simulation techniques in the study of debris motion under extreme coastal conditions. The comprehensive discussion on the currently achievable accuracy of the three modelling approaches will also serve as a benchmark to future developments of numerical model strategies, promoting and strengthening the research community to implement more suitable routines for the complex flow setting, this work considers. In doing so, the results also lay the foundation for more effective disaster management strategies, which holds the potential for far-reaching impacts on coastal communities worldwide.

2 LITERATURE REVIEW

Common guidelines for tsunami-driven debris-field impacts originate from Naito et al. 2014 and Chock 2016, among other seminal works, which were mainly based on a limited set of experiments and case studies. These have certainly seen a significant drive from the Tohoku 2011 tsunami (Yeh et al. 2013) and the Indian Ocean tsunami of 2004 (Merrifield et al. 2005) which both highlighted the limitations

the tsunami debris-field literature had at that time. The study of tsunami-driven debris-fields in a more generalized phenomenon-centered context has been experimentally pursued in recent years using reduced-scale wave flume facilities (Stolle et al. 2016; Goseberg et al. 2016b; Nistor et al. 2017b; Park et al. 2021; Shekhar et al. 2020; Stolle et al. 2020a; Kennedy et al. 2021; Mascarenas 2022; Cinar et al. 2022; Moris et al. 2023) which aim to understand the hazard at a reduced model scale. If done carefully, extrapolation of model-scale conclusions to a prototype tsunami scale may be possible, in particular when spatio-temporal aspects of debris motion are concerned. The investigations on understanding impact loading are experimentally more complex, and require sophisticated instrumentation, often involving multi-axis force sensors, and high-accuracy location tracking of debris (Derschum et al. 2018; Stolle et al. 2018; Stolle et al. 2020b). Several researchers have recently sought to recreate experiments numerically, as in Yang et al. 2017, Hasanpour et al. 2021, Majtan et al. 2022, Hasanpour 2023, Hasanpour et al. 2023, and Bonus 2023, eventually to assist in extrapolating them to prototype scales. These experimental and numerical efforts lead to various attempts to lay the groundwork for scale-invariant and probabilistic design frameworks for tsunami-driven debris-field hazards using probability (Stolle et al. 2020a), such as in their motion (Nistor et al. 2017a), as well as introduction of debris-fields into the modern framework of performance-based engineering analysis in Imai et al. 2022, Bonus et al. 2022, and Bonus 2023 with respect to fire outbreak and structural loading hazards. Although there is no consensus on the most effective and efficient numerical approach to tsunami debris, as identified by Takabatake et al. 2021 and Nistor et al. 2017a, two-way coupled solid-fluid models, smoothed particle hydrodynamics (SPH) and material point method (MPM) schemes show promise and have enjoyed growing popularity. Furthermore, the apparent need for high-resolution 3D debris-fluid-structure interaction models has prompted high-performance multi-CPU and -GPU adoption in open-source tools, notably CB-Geo MPM (Kumar et al. 2019), Karamelo (Nguyen et al. 2023), DualSPHysics (Domínguez et al. 2022), Claymore (Wang et al. 2020), and ClaymoreUW (Bonus 2023).

Comprehensive and extensive multi-physics simulation software, such as STAR-CCM+, are applicable to a wide-range of phenomena and enjoy professional use at scales not truly matched by comparatively academic methods like SPH and MPM. Though SPH is seen increasingly in software like LS-DYNA, it has also begun to occupy the field of coastal and ocean engineering. Open-source SPH code DualSPHysics Domínguez et al. 2022 also supports various wavemaker schemes to assist in wave flume and wave event modeling for coastal hazard analysis (Mitsui et al. 2023). Meanwhile, MPM's primary engineering point of adoption has been geotechnical events involving large-deformations, as in Zhang et al. 2023, Zheng et al. 2021, Tran et al. 2022, Tran et al. 2023, Qiao et al. 2023 and Mast 2013, while its public-facing position has been as a scheme for computers graphics simulations, as in Disney's animated movie Frozen (Stomakhin et al. 2013) and the broader research community which has proposed modifications in Jiang et al. 2015, Fu et al. 2017, Hu et al. 2018, and Fei et al. 2021 for seamless improvement of visuals which offer merit to engineering problems.

MPM and SPH are seen to occupy a similar range of capabilities, both showing strong and weakly-compressible particle method capabilities for a wide range of materials, see Issa et al. 2010 and Chen et al. 2018, but are distinct in their key strengths. MPM finds its stride in simulation of complicated, history-dependent multi-material interaction at large-deformations. However, SPH favors multiphase and free-surface flows with comparatively good pressure-field determination. Only a few comparative studies have been done on SPH versus MPM, leaving a void in a good understanding of where each method has its strength and weaknesses. The most relevant to tsunami debris modelling is Sun et al. 2018, whose authors found both SPH and MPM to be applicable to replication of fluid experiments but noted that MPM is computationally favorable over SPH. This is because it requires no neighbor search algorithm, which tends to scale-up in operations required faster than MPM's particle-grid scatter operations. They also stated that MPM slightly outperforms SPH in accuracy for their fluid cases. We do not personally share the opinion that MPM is superior to SPH for fluids, as they studied small particle counts on implementations that are not fully representative of modern usage of either tool. MPM is commonly in low-order forms proposed by Jiang et al. 2016 and Hu et al. 2018 to achieve high computational performance that may degrade stiff fluid pressures, while SPH is refined for use in high-accuracy fluid simulations needed for shoaling of nonlinear waves and cavitation studies (Altomare et al. 2023). Although this is a generalization on our part, all participants in this manuscript's comparative study consider SPH, not MPM, to be the more logical choice in pure fluid studies. On the contrary, MPM sees better results in collisions of

complex solids versus SPH, as shown by Ma et al. 2009 who found MPM to have an edge over SPH in hyper-velocity impacts, and general large-deformations of complicated solids (e.g., splintering wood, plastic metal, elasto-plastic soils) and mixed phases (e.g. partially liquefied debris-flows) while keeping interactive capability with fluids. This suggests MPM may have untapped potential in quantifying tsunami debris loads on structures or even collapse, which has recently been experimentally covered by Krautwald et al. 2022, assuming the driving fluid can be modeled on-par with SPH. While SPH is not inherently strong for modeling complicated solid materials, there are ways to model non-flowing materials. It is often seen that SPH tools are coupled with the Discrete Element Method (DEM) or the Finite Element Analysis (FEA) to handle solids such as debris and structures. For instance, DualSPHysics by Domínguez et al. 2022 incorporates solids from Project Chrono (Tasora et al. 2016; Martínez-Estévez et al. 2023) which is applied in this manuscript for tsunami debris.

STAR-CCM+ takes a similar approach with coupled rigid bodies used for debris, though its professional and reliable fluid capabilities are far more developed than open-source projects typical in SPH. MPM and STAR-CCM+ do not overlap in their common use, and it may be that they are better seen as compliments than competitors, but we contrast their ability to simulate full tsunami debris wave flume experiments here while noting that coupling high-performance MPM into STAR-CCM+ would be of value.

A critical review of the state of the art in tsunami-debris modeling was provided by Nistor et al. 2017a. Key conclusions include the need to: **(i)** determine appropriate experimental and numerical scales for turbulence (She and Leveque 1994) and debris dynamics (Nistor et al. 2017a), **(ii)** account for robust hydrodynamic boundary conditions numerically, **(iii)** provide rigorous high-resolution studies for 3D model calibration, **(iv)** investigate fundamental debris-debris and debris-fluid behavior in the context of debris entrainment and momentum transfer, **(v)** support of numerical probabilistic approaches (i.e., develop high-performance tools to simulate at higher frequencies) due to the stochastic nature of debris motion, **(vi)** and numerically characterize the demand of multiple debris impact and damming events on structures (Bonus 2023).

All of these studies have pushed the field of numerical tsunami debris modeling forward in their own right. However, challenges persist in high-resolution 3D models (100+ million numerical bodies), multiple debris interactions in fluid-structure deformation and topology changing environments, hyper-elastic and elasto-plastic debris and structural material models, inclusion of air effects such as air pressure build-up, air-water mixing as well as handling arbitrary debris and structure geometries.

This work aims to elucidate some of these issues, demonstrated in a comparative study of three numerical methods investigating five specific comparison objectives: **(i)** hydrodynamics, **(ii)** debris longitudinal displacement, **(iii)** debris lateral spreading angle, **(iv)** characteristic debris-field motion, and **(v)** associated debris loads on structures. Findings herein offer significant value to the fields of coastal engineering and port resource risk management by exposing strengths, weaknesses, and complimentary aspects of these three viable computational approaches. Further, these state-of-the-art, high-performance simulations of meaningful, scaled port settings advance the cutting-edge of numerical tsunami-driven debris-field hazard research for scenarios where port infrastructure are at-risk.

3 FACILITY SPECIFICATIONS

Waseda University's Tsunami Wave Basin flume is a 4 x 9 x 0.5 meter facility featuring adjustable bathymetry, ample overhead access, and a 4 x 0.5 x 1.0 vacuum-pump reservoir with sophisticated computer controls. The flume allows small and mid-scale experiments to control important variables in model's of tsunami events (e.g., spacing of adjacent buildings in a port). This has allowed discovery of empirically tuned equations for predicting chaotic debris motion events, though findings may not extrapolate to prototype events unless considerable effort is employed in similitude control.

Facility details are described in the original experimental paper by Goseberg et al. 2016b, with additional information found in Stolle et al. 2016 and Nistor et al. 2017a. Figure 1 is a schematic of the Tsunami Wave Basin at Waseda University, Tokyo, Japan, as it was configured for the aforementioned experiments. All relevant flume instrumentation information (e.g., location, sampling rate) is aggregated in Table 1. Further description of the flume is noted in the following sections when relevant to assumptions made by respective creators of each numerical digital twin.

4 NUMERICAL METHODS AND DIGITAL TWINS

Table 1. Instrumentation in Waseda University's flume during tsunami-debris experiments and numerical simulations. Instrumentation used in Goseberg et al. 2016b and corresponding positions, operating sampling rate, and meta-data.

Instrument	ID Tag	X	Y	Z	Sample Rate
-	-	[m]	[m]	[m]	[Hz]
WG1	CHT6-30-1	0.00	-2.60	-	100
WG2	CHT6-30-2	-1.75	-0.81	-	100
WG3	CHT6-30-3	-1.75	0.24	-	100
WG4	CHT6-30-4	-1.75	1.70	-	100
ECM1(X)	VMT2-200-04P	-1.65	-0.81	-0.10	100
ECM2(Y)	VMT2-200-04P	-1.65	-0.81	-0.10	100

Table 2. Waseda University Tsunami Wave Basin configuration in the prototype and model. Replication of experiments by Goseberg et al. 2016b in all applied numerical methods. An asterisk, *, denotes that modeler(s) expressed uncertainty in the accuracy of the originally reported experimental value of a parameter. A dagger, †, designates that the associated modeling team performed a parametric study on said parameter.

Parameter	Prototype	Model	Model	Model	Model
Method	-	EXP	MPM	SPH	STAR
Geometric Scale	1:1	1:40	1:40	1:40	1:40
Debris Object	Cargo Container	Smart Debris	Elastic Block	Rigid Block	Rigid Block
Turbulence Model	-	-	Laminar	LES	k-ω SST
Fluid Density (kg/m^3)	1000±3	1000±3	998.0	1000.0	997.561
Fluid Bulk Mod. (Pa)	2.0e9 - 2.3e9	2.0e9 - 2.1e9	2.0e9	3.5e6	Incomp.
Fluid Viscosity (Pa s)	0.8 - 1.1e-3	0.8 - 1.1e-3	1e-3	1e-3	8.8871e-4
Fluid Material	Water	Water	Comp.	Comp.	Incomp.
Still Water Level (m)	9.0	0.23*	0.23	0.23	0.23†
Pressure Head (m)	-	0.67*	0.67	0.67	0.44†
Reservoir Fill (m)	-	0.90*	0.90	0.90	0.67†
Sluice Gate Height (m)	-	0.10*	0.10	0.10	0.10†
Free-Board (m)	1.0	0.025*	0.025	0.025	0.025
Harbor Apron Depth (m)	10.2	0.255	0.255	0.255	0.255
Debris Stiffness (GPa)	0.5 - 1.5	0.5 - 1.5	0.8	-	1.3
Debris Poisson's Ratio	0.25 - 0.45	0.25 - 0.45	0.3	-	0.45
Debris Mass (kg)	14500	0.226	0.226	0.226	0.226
Flume-Debris Restitution	0.30 - 0.60	0.30 - 0.60	-	0.55	0.50
Debris-Debris Restitution	0.40 - 0.70	0.40 - 0.70	-	0.60	0.50
Friction Model	-	-	Coulomb	Coulomb	Coulomb
Flume-Debris Friction	0.15 - 0.80	0.15 - 0.55*	0.45	0.425	0.45
Debris-Debris Friction	0.10 - 0.80	0.05 - 0.35*	-	0.20	0.45
Debris Spacing (m)	1.2	0.03	0.06	0.03	0.03
Debris Length (m)	6.0	0.15	0.15	0.15	0.15
Debris Width (m)	2.4	0.06	0.06	0.06	0.06
Debris Height (m)	2.4	0.06	0.06	0.06	0.06
Column Side-Length (m)	4.0	0.10	0.10	0.10	0.10
Column Spacing X (m)	13	0.325	0.350	0.325	0.325
Column Spacing Y (m)	18	0.450	0.450	0.450	0.450

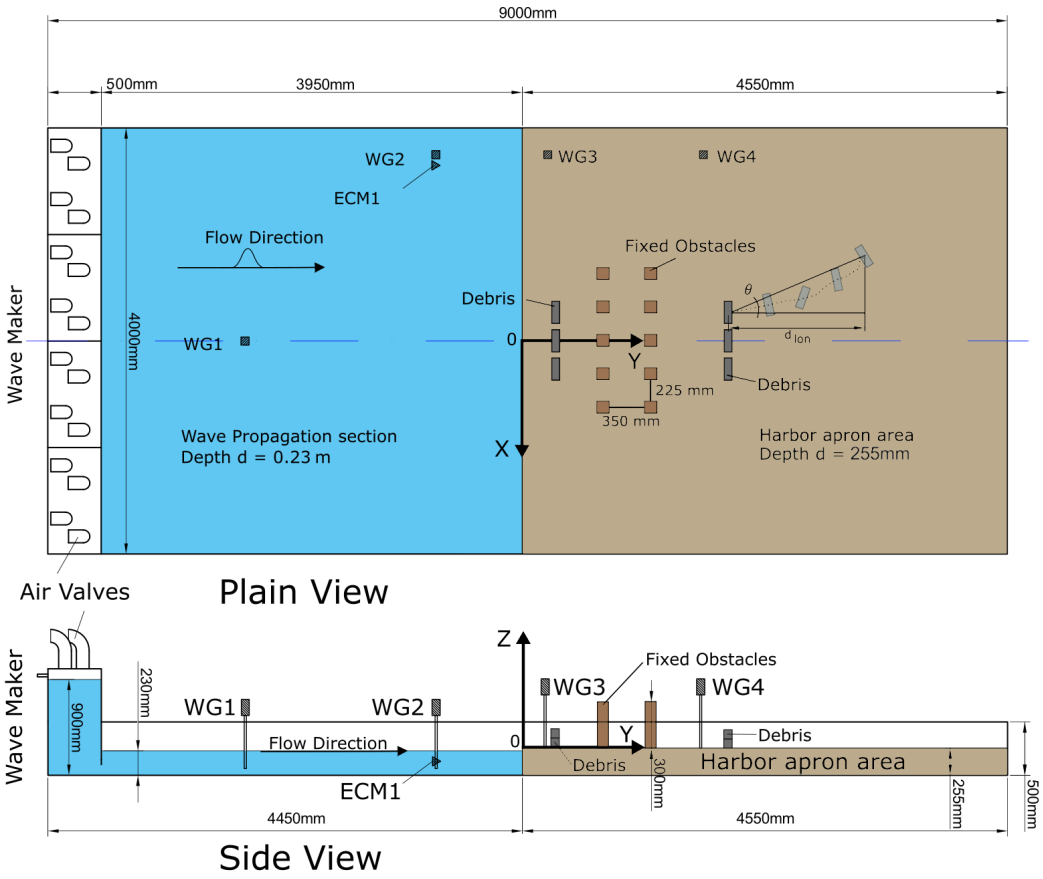

Fig. 1. Schematic of Waseda University's tsunami wave basin, adopted from Goseberg et al. 2016b with original configuration of the experiments, used for our comparative numerical study.

A summary of each of the three numerical method's applied for replication of the debris experiments by Goseberg et al. 2016b is given below. Details on each digital twin model, experiment assumptions, and known limitations of each numerical approach are provided briefly here.

4.1 Material Point Method - ClaymoreUW

The Material Point Method (MPM, Sulsky et al. 1994) is one of the tools chosen to study these flume experiments. We use a Moving-Least-Square Material Point Method (MLS-MPM, Hu et al. 2018) with an assumed deformation volumetric anti-locking scheme (B-Spline F-Bar, Zhao et al. 2023) with custom modifications discussed in Bonus 2023 for improved stability and compatibility with the G2P2G fused kernel (Wang et al. 2020) used in ClaymoreUW's MLS-MPM implementation. Primary digital twin parameters are included in Table 2 and Table 1, with further exposition below.

Governing Equations

The traditional approach (Sulsky et al. 1993) is built around conservation of linear momentum, which when expressed in differential form appears as follows:

$$\rho\,\dot{\mathbf{v}} = \nabla \cdot \sigma + \mathbf{b}\ , \tag{1}$$

with the mass density $\rho(\mathbf{x}, t)$ at position $\mathbf{x}$ and time t, $\dot{\mathbf{v}}(\mathbf{x}, t)$ as the material time derivative of the velocity field—also known as the acceleration field. Stress divergence $\nabla \cdot \sigma$, where ∇ the gradient operator, $\sigma(\mathbf{x}, t)$ is the Cauchy stress tensor. $\mathbf{b}(\mathbf{x}, t)$ is the body force per unit volume.

In short, the Material Point Method formulation used herein applies Cauchy's momentum equation with mass conservation and reserves the capability for full constitutive law variation. In turn, the method

super-sets the governing equations rooted in both compressible and imcompressible Navier-Stokes, as they do not allow for material variation via constitutive laws without coupling to complimentary methods.

Boundary Conditions

The Material Point Method (MPM) applies boundary conditions to its shared grid (i.e. a mass and velocity field). Because the grid is shared and automatically handles multi-phase and multi-material interaction, applying BCs here holds the property invariant and is thereby extremely valuable. MPM typically uses a uniform Cartesian grid (i.e. evenly spaced grid with cells making squares or bricks for 2D or 3D). This further simplifies boundary conditions if boundaries align with the grid. However, scene boundaries that do not perfectly align with the MPM grid often occur, resulting in MPM errors proportional to grid-spacing (Δx). This is a limitation of all MPM implementations unless more advanced methods are used. Keeping this in mind, a projection operator (**Proj**) (Hu et al. 2018) for boundary conditions used in our code can be broadly stated as:

$$\mathbf{v}_i^* = \mathbf{Proj}(\mathbf{v}_i, \mathbf{n}_i, \mathcal{B}, \mu_c) = \begin{cases} \mathbf{0} & \text{where } \mathcal{B} \text{ is sticky,} \\ \mathbf{v}_t & \text{where } \mathcal{B} \text{ is slip,} \\ \zeta \mathbf{v}_t & \text{where } \mathcal{B} \text{ is separate and } \mathbf{v}_r \cdot \mathbf{n}_i \leq 0, \\ \mathbf{v}_i & \text{where } \mathcal{B} \text{ is separate and } \mathbf{v}_r \cdot \mathbf{n}_i > 0 \ , \end{cases} \tag{2}$$

where $\mathcal{B}$ is the boundary type (e.g. sticky, slip, separable), $\mathbf{v}_i$ is the grid-node velocity, $\mathbf{v}_b$ is the boundary velocity, $\mathbf{v}_r$ is relative velocity ($\mathbf{v}_r = \mathbf{v}_b - \mathbf{v}_i$), $\mathbf{n}_i$ is the boundary surface normal on the grid-node, $\mathbf{v}_t$ is relative velocity tangent to the boundary ($\mathbf{v}_t = \mathbf{v}_r - \mathbf{v}_r \cdot \mathbf{n}_i$), μ_c is a Coulomb friction parameter (either static or dynamic), and ζ is a tangential contact factor (i.e. set using μ_c).

We model the flume walls, harbor, and obstacles as rigid boundaries with separable velocity conditions on the MPM background grid. The reservoir panel separating the main flume and the water reservoir fluid is taken as 0.04 m thick to avoid fluid particle interaction across the barrier. The reservoir opening, i.e., sluice gate, is a 0.10 m gap in the boundary condition that separates the reservoir wall from the flume's base. The vertical quay harbor wall, i.e., the front panel separating the water basin and the dry harbor apron, is 0.255 m high and applies a separable velocity boundary condition on streamwise flow only. The harbor apron is flat and applies a separable velocity condition. The floor applies a Coulomb static and dynamic friction coefficient of 0.45 to orthogonal velocity if there are debris particles nearby. This is to ensure the friction is local to the debris-floor interface. The harbor apron continues over 4.55 m to reach the flume's back wall, which has a separable condition to allow wave reflection. The square column obstacles are placed as in Goseberg et al. 2016b, although we increase the transverse spacing from 0.325 m to 0.350 m to maintain grid-alignment while accounting for the added spacing between debris. Load-cells are numerically set on the leading face of obstacles, recording the forces imposed streamwise on rigid boundary grid nodes. Although the experiments did not have load-cells on obstacles, instead using 30 Hz accelerometer data from debris bodies, we model them here as we were interested in evaluating the quality and content of motion-based debris impact force data compared to a more direct load measurements on structures. Sampling rate is set to 1200 Hz to capture stiff impacts.

Numerical Schemes

We modify the B-Spline F-Bar volumetric antilocking scheme by Zhao et al. 2023 to use a linear mixing ratio, $\psi \in [0, 1]$, for an adjustable balance of pressure field smoothness and low-dissipation stabilization. This linear combination of B-Spline F-Bar in an explicit MPM appears in Bonus 2023 with additional exposition. Our antilocking mixing approach is reminiscent structurally to the PIC-FLIP velocity mixing popularized in graphics communities by Zhu and Bridson 2005 and Stomakhin et al. 2013. The assumed deformation gradient determinant ($\bar{J}$) on a particle (p) at a time step (n) for the stress update is defined as:

$$\bar{J}_p^{n+1} = (\psi) \sum_i N_{ip} \bar{J}_i + (1 - \psi) \left(J_p^n \Delta J_p \right) \tag{3}$$

$$= (\psi) \, \Pi \left(\bar{J}_p^n \Delta J_p \right) + (1 - \psi) \left(J_p^{n+1} \right) \ , \tag{4}$$

where Π is the grid-averaging projection operator from Zhao et al. 2023. This simply adds a weighted grid-averaged deformation gradient from Zhao et al. 2023 to the counter-weighted deformation gradient determinant of standard MPM or MLS-MPM. For $\psi = 0$, the scheme reduces to standard MPM or MLS-MPM. For $\psi = 1$, the scheme becomes that of Zhao et al. 2023. Typical ψ values we use for stiff fluid simulations are between $\psi = 0.9$ to 0.9999, with 0.9999 selected for all MPM cases in this manuscript.

Initial Conditions

Water is modeled with a mixed-precision, high-accuracy, high-performance PA-JB fluid formulation (Precision-Accelerated J-Bar fluid, see Bonus 2023). It is mathematically identical to the common isotropic weakly-compressible fluid using the Murnaghan-Tait equation of state, from Murnaghan 1944 and Tait 1888, with inclusion of dynamic viscous stress as it was applied in Pradhana et al. 2017. The PA-JB fluid model improves both accuracy and speed on multi-GPUs platforms while using less memory and smaller device-to-device memory transfers. This provides significant benefits as our simulations use a minimum of 75 million fluid particles undergoing 4 million time-steps on two GPU. Density (ρ_w) of the fluid is 998 kg m^{-3} and bulk modulus (B_w) is 2.0 GPa which correspond to a speed-of-sound (c_w) of 1415 m s^{-1}. Viscosity (μ_w) is 1.0 cP (0.001 Pa $\times$ s). The polytropic constant (γ_w) is 7.125, which is often interpreted as the bulk modulis' derivative with respect to pressure at sea-level (Tait 1888). No turbulence model is applied. The still water level (h_{SWL}) is set to 0.23 m and water elevation in the reservoir ($h_{Res.}$) is 0.9 m. No initial pressure field is used, rather gravity loads the fluid suddenly with a magnitude of $-9.806\,65$ m s^{-2} when the simulation begins. F-Bar volumetric antilocking (Zhao et al. 2023) is used for water particles to improve the pressure field, which otherwise may behave overly stiff. We include a linear mixing coefficient ($\psi_w = 0.9999$), as described in Bonus 2023, for stability and accuracy.

Debris are modeled as double-precision fixed-corotated solids (Jiang et al. 2016), which is equivalent to common Neo-Hookean formulations at small-strains. We modeled debris as solid blocks rather than hollow ones with internal supports to avoid thin walls defined by only 2 particles, which are not reliable in bending at impact. Debris density (ρ_d) is set to 419 kg m^{-3}, instead of 921 kg m^{-3}, to account for this internal geometry change. Poisson ratio (ν_d) is 0.3 and Young's modulus (E_d) is 0.8 GPa to replicate typical HDPE plastic.

Parallel Scaling and Hardware Used

Our digital twin is simulated in mixed-precision. The grid uses single-precision, while the particles use mixed and double-precision floating computations. MPM simulations are executed on Texas A&M University's high-performance computing cluster for Accelerating Computing for Emerging Sciences (TAMU ACES), but are also tested Texas Advanced Computing Center's Frontera and Lonestar6 systems in single and mixed floating point precision, respectively.

Computational time was reserved through the NSF ACCESS program and DesignSafe-CI. One node was used per simulation, with said node possessing 256 GB RAM, two Intel Xeon 8468 Sapphire Rapids processors @ 3.80 GHz with 48 physical cores for a combined total of 96 physical cores across two sockets, and two NVIDIA H100 PCIe Graphics Processing Units (GPU) with 80 GB of global video memory each. The calculation of the 12.5 s simulation time for the wave flume with a half lateral extent, consisting of approximately 75×10^6 particles undergoing roughly 4×10^6 time-steps (i.e., 3×10^{13} total executions of the mixed/double-precision MPM particle algorithm per simulation), took an average of 1.25 d in HydroUQ's ClaymoreUW MPM module, which was built locally on the Ubuntu 18.04-LTS operating system, i.e., a 2.4 h s^{-1} computation-to-simulated time ratio. Note that simulations use explicit time-stepping while applying a realistic water bulk modulus, which often amplifies total computational time by orders of magnitude compared to approaches using artificially reduced bulk moduli (a common occurrence in MPM and SPH studies), yet still complete in almost a single day because of the excellent scaling properties of the multi-GPU-accelerated MPM software. Further, we primarily use double-precision computations with a handful of mixed-precision optimizations, which may take 1.5 $\times$ to 32 $\times$ longer for NVIDIA GPU hardware to compute than a case using only single-precision floating-point operations.

4.2 Smoothed Particle Hydrodynamics - DualSPHysics

DualSPHysics employs a weakly compressible SPH methodology within a comprehensive computational toolbox that encompasses solid mechanics and multiphase modeling (Domínguez et al. 2022).

Initially designed for the investigation of coastal engineering problems, the toolbox provides numerous wave generation techniques, with additional capabilities to investigate flow problems.

Governing Equations

The SPH method approximates any function F for a particle a based on the weighted set of neighboring particles b confined within the region defined by a smoothing length h which was set to $\sqrt{3}$ times the initial particle spacing Δ. Weights are assigned through an inverse distance function with the distance $\vec{r}$ between particles defined as $\vec{r}_{ab} = \vec{r}_b - \vec{r}_a$, the smoothing kernel W, times the neighbor volumes V_b:

$$F(\vec{r}_a) \approx \sum_b F(\vec{r}_b) V_b W(\vec{r}_a - \vec{r}_b, h), \text{ with } V_b = \frac{m_b}{\rho_b}. \tag{5}$$

The constant mass of a particle is defined by m and ρ is the varying mass density of a particle. In this study, the quintic Wendland kernel function (Wendland 1995) defines the weight of neighboring particles:

$$W(\|\vec{r}\|, h) = \alpha_D \left(1 - \frac{q}{2}\right)^4 (2q+1), \text{ with } q = r/h \text{ and } 0 \le q \le 2. \tag{6}$$

Here r is the absolute distance in between any particle a and the neighboring particle b and $\alpha_d = 21/16\pi h^3$. The mass continuity is calculated with

$$\frac{d\vec{\rho}_a}{dt} = \rho_a \sum_b \frac{m_b}{\rho_b} \vec{v}_{ab} \cdot \nabla_a W_{ab} + DDT. \tag{7}$$

The time is defined through t, $\vec{v}$ is the particle velocity and DDT represents any density diffusion term applied throughout the simulations. The conservation of momentum

$$\frac{d\vec{v}}{dt} = -\frac{1}{\rho}\nabla P + \vec{g} + \vec{\Gamma} \tag{8}$$

, with the fluid pressure P, the gravitational acceleration $\vec{g} = (0.0, 0.0, -9.81)\ \mathrm{m\,s^{-2}}$ relative to the still-water's surface normal (i.e. the Z axis) and a dissipative term $\vec{\Gamma}$, which is formulated to account for viscous transport. In this study, the kinematic viscosity ν and an eddy viscosity ν_t are used to account for viscous transport of the resolved and unresolved flow field. The discretized equation is

$$\begin{aligned} \frac{d\vec{v}_a}{dt} = &\sum_b m_b \left(\frac{P_b \cdot P_a}{\rho_b \cdot \rho_a}\right) \nabla_a W_{ab} + \vec{g} \\ &+ \sum_b m_b \left(\frac{4\nu r_{ab} \cdot \nabla_a W_{ab}}{(\rho_a + \rho_a)\left(r_{ab}^2 + 0.01h^2\right)}\right) \vec{v}_{ab} \\ &+ \sum_b m_b \left(\frac{\tau_{ij}^b}{\rho_b^2} + \frac{\tau_{ij}^a}{\rho_a^2}\right) \nabla_a W_{ab}. \end{aligned} \tag{9}$$

(10)

In this study ν in Equation 10 has a value of $1.0 \times 10^{-6}\ \mathrm{m^2\,s^{-1}}$ and τ_{ij} is an element of the stress tensor based on Einstein notation. The sub-particle stress tensor $\vec{\tau_{ij}}$ divided by the density ρ is defined by

$$\frac{\vec{\tau_{ij}}}{\rho} = \nu_t \left(2S_{ij} - \frac{2}{3}S_{ii}\delta_{ij}\right) - \frac{2}{3}C_I \Delta^2 \delta_{ij} |S_{ij}|^2. \tag{11}$$

δ_{ij} is the Kronecker delta and $C_I = 0.0066$. The eddy viscosity ν_t is based on the Smagorinsky model

$$\nu_t = (C_s \Delta l)^2 \sqrt{2S_{ij}S_{ij}}, \text{ with } S_{ij} = -\frac{1}{2}\left(\frac{du_i}{dx_j} + \frac{du_j}{dx_i}\right). \tag{12}$$

Δl is the instantaneous particle spacing and the Samgorinsky coefficient C_s is set to $C_s = 0.12$ (Dalrymple and Rogers 2006). An equation of state for a weakly compressible fluid is used to calculate the fluid pressure:

$$P = c_0^2 \frac{\rho_0}{\gamma_w} \left[\left(\frac{\rho}{\rho_0} \right)^{\gamma_w} - 1 \right], \text{ with } \gamma_w = 7. \tag{13}$$

c_0 is the speed of sound for the reference density of water $\rho_0 = 1000\,\mathrm{kg\,m^{-3}}$ and γ_w is the polytropic constant of water. The speed of sound c_0 was fixed at $60\,\mathrm{m\,s^{-1}}$, corresponding to a bulk modulus of 3.5 MPa for a fixed density, which was approximately twenty times the observed maximum flow velocity. A value of at least ten times the maximum flow velocity is frequently used, as density variations remain consistent for such a value (Monaghan 1994; Monaghan and Kos 1999). Doubling the speed of sound approximately doubled the computational run time. Therefore, The value of $60\,\mathrm{m\,s^{-1}}$ is chosen as a trade-off in between accuracy of the pressure field and computational costs.

In DualSPHysics the fluid forces are calculated based on the sum of the neighboring solid particles defined by both the kernel function and the smoothing length. Every solid, movable object is represented by a set of particles which keep their relative positions to another during the simulation. Once a boundary particle k interacts with fluid particles, a force per unit mass f is exerted on the particle k given by

$$\vec{f}_k = \sum_c \vec{f}_{kc}. \tag{14}$$

$\vec{f}_{kc}$ is the force per units mass from each interacting fluid particle c onto the solid particle k based on global coordinates. Debris is modeled through the multiphysics library Chrono as described in Martínez-Estévez et al. 2023. In this study, the DEM-approach that is expanded by a differential variational inequality approach to enforce non-penetration of debris particles (Anitescu and Tasora 2010) is applied. It is also known in general as DEM-C or non-smooth contact modelling in DualSPHysics. Interaction of rigid objects is modelled with a Coulomb friction model and a restitution coefficient to account for parallel and normal forces (Johnson 1985). Project Chrono is using generalized position coordinates $\vec{q}$. The time derivatives of $\vec{q}$ are then defined through a linear transformation Matrix $\vec{\Gamma}$ times of the generalized velocities $\vec{v_q}$:

$$\frac{d\vec{q}}{dt} = \vec{\Gamma}\left(\vec{q}\right) \vec{v}_q. \tag{15}$$

The force balance of debris is defined as

$$\vec{M} \frac{d\vec{v_q}}{dt} = \sum_{i=1,2,\ldots,p}^{p} \left(\hat{\gamma}_n^i \vec{D_n^i} + \hat{\gamma}_u^i \vec{D_u^i} + \hat{\gamma}_v^i \vec{D_v^i} \right) + \vec{f_e}\left(t, \vec{q}, \vec{v}_q\right) - \vec{f_c}\left(t, \vec{q}\right). \tag{16}$$

Here $\vec{M}$ is the constant mass matrix. $\hat{\gamma_n}$ is the restitution coefficient and $\hat{\gamma_u}$ and $\hat{\gamma_v}$ are the friction coefficients. D is a projector to achieve generalized contact forces for each contact i of all contacts p, where a contact is defined as the interaction of two solids. $\vec{f_e}$ are all external forces of Equation 14 in generalized form and $\vec{f_c}$ are all constraining forces. $\vec{f_c}$ would be non-zero in systems using constraints, such as joints or hinges, not applied in this study. $\hat{\gamma}_n^i$ is fulfilling

$$\hat{\gamma}_n^i \geq 0 \perp \Phi i \geq 0\,,\, i = 1, 2, ..., p\,, \tag{17}$$

with Φ being the gap function defined as

$$\Phi\left(q\right) = \begin{cases} > 0 & \text{, if two solids are separated} \\ = 0 & \text{, if two solids are in contact} \\ < 0 & \text{, if two solids are in interpenetrating} \end{cases}. \tag{18}$$

The tangential force factors are then defined by

$$\left(\hat{\gamma}_u^i, \hat{\gamma}_v^i\right) = \underset{\mu^i \hat{\gamma}_n^i \geq \sqrt{\left(\hat{\gamma}_u^i\right)^2 + \left(\hat{\gamma}_u^i\right)^2}}{\operatorname{argmin}} \left(\hat{\gamma}_u^i \vec{D}_u^i + \hat{\gamma}_v^i \vec{D}_v^i\right) \ , i = 1, 2, ..., p. \tag{19}$$

In this context, μ is the uniform friction coefficient applied in the model. Chronos Coulomb friction model does not distinguish friction coefficients into static and kinetic friction coefficients or provides an option for directional dependence. Solid-solid interaction is initiated for solids that are one initial particle distance of $\Delta = 0.005$ m apart.

Numerical Schemes

The explicit symplectic position Verlet time integrator scheme (Leimkuhler and Matthews 2015) is used for time integrator solving. Adaptive time stepping with a CFL-number of 0.3 is applied for all particles. A density diffusion of Fourtakas et al. 2020 is applied in all simulations for pressure stabilization. Therefore, DDT in Equation 13 is equal to

$$DDT = \delta_\Phi h c_0 \sum_b \Psi_{ab} \cdot \nabla_a W_{ab} V_b. \tag{20}$$

In this context, δ_Φ is a coefficient that was kept at a value of 0.1 throughout all simulations and Ψ_{ab} is defined by

$$\Psi_{ab} = 2\left(\rho_{ab}^T - \rho_{ab}^H\right) \frac{\vec{x}_{ab}}{\|\vec{x}_{ab}\|^2}, \text{ with } \rho_{ab}^H = \rho_0 \left(\gamma_w \sqrt{\frac{\rho_0 g z_{ab} + 1}{\frac{c_0^2 \rho_0}{\gamma_w}}} - 1 \right). \tag{21}$$

Here, ρ^T is the total density of a particle, ρ^H is the hydrostatic component of the density of a particle, $\vec{x}$ is the particle position vector and z the vertical position of the particle. Additionally, to increase the homogeneity of spatial particle distribution, an additional diffusion term is added in the framework of particle shifting as described by Lind et al. 2012. Particles shifting transports particles into areas of lower particle concentration to minimize gaps in the flow field. The diffusion vector $\delta\vec{r}_s$ is determined through

$$\delta\vec{r}_s = \begin{cases} -\frac{\nabla \cdot \vec{r} - 2.75}{0.25} A h \|\vec{u}\|_i dt \sum_j V_j \nabla W_{ij} & \text{, if } \nabla \cdot \vec{r} - 2.75 < 0 \\ -A h \|\vec{u}\|_i dt \sum_j V_j \nabla W_{ij} & \text{, if } \nabla \cdot \vec{r} - 2.75 = 0 \end{cases} \tag{22}$$

The first case is applied around the free surface, while the second case is applied everywhere else. The coefficient A was kept at a value of 2 during all simulations.

Boundary Conditions

Fluid-boundary interaction was achieved through the modified dynamic boundary condition (mDBC) (English et al. 2022) with three layers of boundary particles for debris, obstacles and wave flume to increase accuracy of fluid-structure interaction (FSI). A zero velocity without roughness effects is set at the boundary particles. The mDBC improves fluid-boundary interaction in comparison with the standard dynamic boundary condition implementation given by (Crespo et al. 2007). A friction coefficient of 0.425 and a restitution coefficient of 0.55 is used for the interaction of stationary wave flume and plastic containers inside the Chrono framework. For the interaction of plastic containers with each other, a friction coefficient of 0.2 and a restitution coefficient of 0.6 are used.

In prior internal investigations, which were not published, the setup delineated by Goseberg et al. 2016b was investigated using Eulerian multiphase solvers through the DualSPHphysics workgroup aside from the analysis employing DualSPHysics. All analyses indicated a discernible time-varying inflow of air through the air valves. The initial bore's maximum water surface was found to be overestimated when considering only the influence of gravity on the water column. To address this, a dynamic vertical acceleration, varying with time, is implemented on the water column above the still water level within the reservoir due to a lack of options regarding a pressure decay inside the reservoir. This serves to impede the outflow of water and reduce the water surface elevation of the initial bore. The affected water column consists of all particles up to a height of 0.67 m above the still water level, as sketched in sub-plot (A) of Figure 2. The detailed characteristics of the calibrated time-dependent acceleration are given in sub-plot (B) of Figure 2. The determination of the acceleration profile involved an iterative fitting process in

two-dimensional simulations of the scenario depicted in Figure 1, with no consideration given to debris or obstacles. The calibration procedure relied on hydrodynamics data associated with WG1.

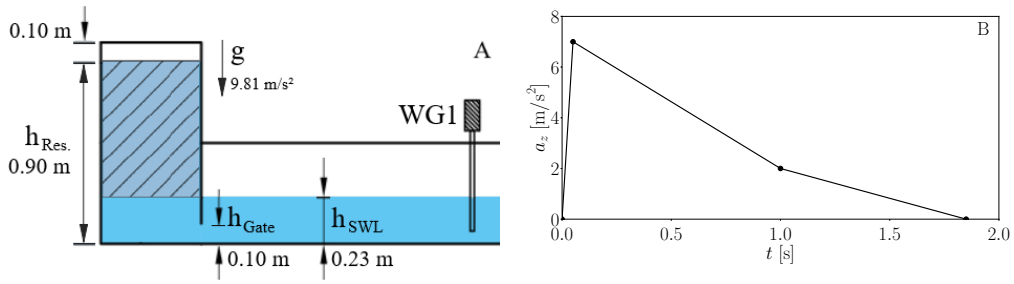

Fig. 2. Empirical acceleration adjustments inside the reservoir. **(A)** For SPH simulations, water (solid blue) that is both above the h_{SWL}=0.23 m SWL and inside the reservoir (hatched blue) has an empirically tuned vertical acceleration adjustment, a_z. This is to replicate the first wave crest of the wave train and the elongated flow from experiments by Goseberg et al. 2016b; **(B)** Magnitude of the empirical vertical acceleration adjustment, a_z, used in the reservoir for SPH simulations.

Initial Conditions

The initial particle spacing Δ amounted to 0.005 m. The still water level inside the basin was set to 0.230 m, while the water level inside the reservoir amounted to 0.9 m. Debris were modelled as solid rectangular objects with a mass of 0.226 kg. DualSPHysics adapts the mass of all bounding particles such that the total mass of the debris is equal to 0.226 kg. A minor deviation of the vertical position of the center of mass in comparison with the experiment of Goseberg et al. 2016b is therefore present, as the internal geometry of the smart debris is not completely symmetrical. Debris had dimensions of LxWxH equal to 0.15 m x 0.06 m x 0.06 m. Street width in x and y direction amounted to 0.225 m and 0.35 m, respectively. Stacked debris were initially one particle distance of Δ = 0.005 m apart. The whole wave basin with a length of 9.0 m and a width of 4.0 m were modelled, with walls present at each boundary.

Software Specifics and Implementation

Single precision is used throughout all simulations, as double precision was not found to significantly alter results while increasing the computing time.

Parallel Scaling and Hardware Used

The simulations were run on a local desktop computer with 16 GB RAM, an Intel Core i7-4790 CPU running at 3.60 GHz and 8 physical cores with 2 threads per core, and an NVIDIA GeForce RTX 3090 Graphics Processing Unit (GPU) running at a base clock speed of 1.395 GHz with a memory size of 24 GB. The calculation of the 10 s simulation time for the wave flume with a full lateral extent, consisting of approximately 50×10^6 particles, took an average of 3.2 d (i.e., a 7.68 h s^{-1} computation-to-simulated time ratio) in DualSPHysics.

All simulations setups are available at the publication service LeoPARD of the Technische Universität Braunschweig: DOI.

4.3 Computational Fluid Dynamics - Simcenter STAR-CCM+

Siemens' Simcenter STAR-CCM+ offers a full suite of multiphysics CFD simulation solvers covering single-phase, multiphase, and particle flows, heat transfer, solid mechanics, aeroacoustics, FSI, reacting flows, electromagnetics, and rheology (Siemens Digital Industries Software 2023a). The majority of these solvers are based upon the Finite Volume Method (FVM), but alternative methods are utilized for specific cases. For instance, the FEM is used for solid mechanics, the DEM provides complex particle interaction capabilities, and the Harmonic Balance Method (HBM) is suitable for periodically-repeating fluid flows (e.g., turbomachinery) and electrodynamics applications with harmonic time dependence.

Governing Equations

To simulate the water-air interactions of the free-surface fluid flow of the tsunami-like waves generated in the Waseda University wave flume, the unsteady Reynolds-Averaged Navier-Stokes (URANS) form of the continuity and momentum equations for a Newtonian fluid were utilized along with the VOF multiphase flow model developed by Hirt and Nichols 1981. To derive the RANS equations, each flow field variable, ϕ, including the velocity components, pressure, and energy for this research, must be decomposed into mean, $\overline{\phi}$, and fluctuating terms, ϕ', as follows.

$$\phi = \overline{\phi} + \phi' \tag{23}$$

Substituting this variable decomposition into the Navier-Stokes equations allows for simplifying them to their RANS form, where ρ is density, $\overline{\mathbf{u}}$ is the mean velocity vector, $\overline{p}_{\text{mod}} = \overline{p} + \frac{2}{3}\rho k$ is the modified mean pressure with $\overline{p}$ and $k = \frac{1}{2}\mathbf{u}' \cdot \mathbf{u}'$ being the mean pressure and turbulent kinetic energy, $\mathbf{u}'$ is the fluctuating velocity vector, $\mathbf{I}$ is the identity tensor, $\overline{\mathbf{T}}$ is the mean viscous stress tensor, f_b is the body force vector, $\overline{E}$ is the mean total energy per unit mass, and $\overline{\mathbf{q}}$ is the mean heat flux vector.

$$\frac{\partial \rho}{\partial t} + \nabla \cdot (\rho \overline{\mathbf{u}}) \tag{24}$$

$$\frac{\partial \rho \overline{\mathbf{u}}}{\partial t} + \nabla \cdot (\rho \overline{\mathbf{u}} \otimes \overline{\mathbf{u}}) = -\nabla \cdot (\overline{p}_{\text{mod}} \mathbf{I}) + \nabla \cdot (\overline{T} + \overline{\mathbf{T}}_{\text{RANS}}) + \mathbf{f}_b \tag{25}$$

$$\frac{\partial \rho \overline{\mathbf{E}}}{\partial t} + \nabla \cdot (\rho \overline{E} \overline{\mathbf{u}}) = -\nabla \cdot (\overline{p}_{\text{mod}} \overline{\mathbf{u}}) + \nabla \cdot (\overline{T} + \overline{\mathbf{T}}_{\text{RANS}}) \overline{\mathbf{u}} + \nabla \cdot \overline{\mathbf{q}} + \mathbf{f}_b \overline{\mathbf{u}} \tag{26}$$

Turbulence modeling was incorporated using a RANS type of model. In particular, the k-ω Shear Stress Transport (SST) model developed by Menter 1993 was selected for its superior capabilities at simulating strongly separated flows such as tsunami wave impacts and inundation flows around bluff bodies including buildings and bridges, as was demonstrated by Winter 2019. The k-ω SST model also avoids downsides of using a single model through blending of the k-ε and k-ω models such that k-ε is used in the far field away from boundaries to avoid issues caused by the k-ω model's sensitivity to the degree of turbulence in the free stream, whereas k-ω is used near boundaries to avoid spurious generation of turbulent kinetic energy (TKE), from which k-ε models are known to suffer, especially near stagnation points (Siemens Digital Industries Software 2023b; Rumsey et al. 2006). Such models are incorporated as system of equation closures that provide a definition for the Reynolds stress tensor, $\mathbf{T}_{\text{RANS}}$, in addition to adding further transport equations. More specifically, the k-ω SST model falls into the class of turbulence models referred to as eddy viscosity models, which incorporate a turbulent eddy viscosity, μ_t. This type of model makes use of the Boussinesq approximation, defining the Reynolds stress tensor as follows, where $\mathbf{S} = \frac{1}{2}(\nabla \overline{\mathbf{u}} + \nabla \overline{\mathbf{u}}^T)$ is the mean strain rate tensor.

$$\mathbf{T}_{\text{RANS}} = 2\mu_t \mathbf{S} - \frac{2}{3}\mu_t (\nabla \cdot \overline{\mathbf{u}}) \mathbf{I} \tag{27}$$

The key differences between such turbulence models lie in how they define the turbulent eddy viscosity as well as in model coefficient values. The general form of the turbulent eddy viscosity in STAR-CCM+ for all k-ω type models is as follows, where T is the turbulent time scale.

$$\mu_t = \rho k T \tag{28}$$

Without enabling either of the Durbin Scale or Vorticity Limiter Realizability options for the k-ω SST model, the turbulent time scale is defined as shown below, where $\alpha^* = F_1 \alpha_1^* + (1 - F_1)\alpha_2^*$, $\alpha_1^* = 1$, $\alpha_2^* = 1$, ω is the specific dissipation rate, $a_1 = 0.31$, and $C_T = 0.6$ are model coefficients, $S = \sqrt{2\mathbf{S} : \mathbf{S}}$ is the modulus of the mean strain rate tensor, and F_1 and F_2 are blending functions.

$$T = \min\left(\frac{\alpha^*}{\omega}, \frac{a_1}{S F_2}\right) \tag{29}$$

The blending functions F_1 and F_2 are defined according to the subsequent equations, where $\beta^* = 0.09$ is a model coefficient, d is the wall distance, ν is the kinematic viscosity, and $CD_{k\omega} = \max(\nabla k \cdot \nabla\omega/\omega, 10^{-20})$ is the cross-diffusion coefficient.

$$F_1 = \tanh\left(\left[\min\left(\max\left(\frac{\sqrt{k}}{0.09\omega d}, \frac{500\nu}{\omega d^2}\right), \frac{2k}{CD_{k\omega}d^2}\right)\right]^4\right) \tag{30}$$

$$F_2 = \tanh\left(\left[\max\left(\frac{2\sqrt{k}}{\beta^*\omega d}, \frac{500\nu}{\omega d^2}\right)\right]^2\right) \tag{31}$$

The k-ω SST model is considered a two-equation RANS eddy viscosity model since it incorporates two additional transport equations, one each for the turbulent kinetic energy, k, and the specific dissipation rate, ω, where μ is the dynamic viscosity, $\sigma_k = F_1\sigma_{k1} + (1 - F_1)\sigma_{k2}$, $\sigma_{k1} = 0.85$, $\sigma_{k2} = 1$, $\sigma_\omega = F_1\sigma_{\omega1} + (1 - F_1)\sigma_{\omega2}$, $\sigma_{\omega1} = 0.5$, and $\sigma_{\omega2} = 0.856$ are model coefficients, P_k and P_ω are production terms, f_{β^*} is the free-shear modification factor, f_β is the vortex-stretching modification factor, S_k and S_ω are user-specified source terms, and k_0 and ω_0 are ambient turbulence values that counteract turbulence decay.

$$\frac{\partial\rho k}{\partial t} + \nabla\cdot(\rho k\overline{\mathbf{u}}) = \nabla\cdot\left[(\mu + \sigma_k\mu_t)\nabla k\right] + P_k - \rho\beta^* f_{\beta^*}(\omega k - \omega_0 k_0) + S_k \tag{32}$$

$$\frac{\partial\rho\omega}{\partial t} + \nabla\cdot(\rho\omega\overline{\mathbf{u}}) = \nabla\cdot\left[(\mu + \sigma_\omega\mu_t)\nabla\omega\right] + P_\omega - \rho\beta f_\beta(\omega^2 - \omega_0^2) + S_\omega \tag{33}$$

The production terms are defined as follows, where G_k is the turbulent production, G_b is the buoyancy production, G_{nl} is the non-linear production, G_ω is the specific dissipation production, D_ω is the cross-diffusion term, f_c is the curvature correction factor, $\beta = F_1\beta_1 + (1 - F_1)\beta_2$ is the coefficient of thermal expansion, $\beta_1 = 0.075$ and $\beta_2 = 0.0828$ are model coefficients, Pr_t is the turbulent Prandtl number, $\overline{T}$ is the mean temperature, $\mathbf{g}$ is the gravitational acceleration vector, $\mathbf{T}_{\text{RANS,NL}}$ is a non-linear constitutive relation (e.g., either quadratic or cubic, which are higher-order than the linear Boussinesq approximation, if enabled in STAR-CCM+), $\gamma = F_1\gamma_1 + (1 - F_1)\gamma_2$, $\gamma_1 = \beta_1/\beta^* - \sigma_{\omega1}\kappa^2/\sqrt{\beta^*}$, and $\gamma_2 = \beta_2/\beta^* - \sigma_{\omega2}\kappa^2/\sqrt{\beta^*}$ are model coefficients, and $\kappa = 0.41$ is the von Kármán constant.

$$P_k = G_k + G_b + G_{nl} \tag{34}$$

$$G_k = \mu_t f_c S^2 - \frac{2}{3}\left(\rho k\nabla\cdot\overline{\mathbf{u}} + \mu_t(\nabla\cdot\overline{\mathbf{u}})^2\right) \tag{35}$$

$$G_b = \frac{\beta\mu_t}{Pr_t}\left(\nabla\overline{T}\cdot\mathbf{g}\right) \tag{36}$$

$$G_{nl} = \mathbf{T}_{\text{RANS,NL}} : \nabla\overline{\mathbf{u}} \tag{37}$$

$$P_\omega = G_\omega + D_\omega \tag{38}$$

$$G_\omega = \rho\gamma\left(S^2 - \frac{2}{3}(\nabla\cdot\overline{\mathbf{u}})^2 - \frac{2}{3}\omega\nabla\cdot\overline{\mathbf{u}}\right) \tag{39}$$

$$D_\omega = \frac{2\rho(1 - F_1)\sigma_{\omega_2}}{\omega}\left(\nabla k\cdot\nabla\omega\right) \tag{40}$$

The curvature factor applied in the turbulent production term G_k is defined by the following equation, where $C_{\max} = 1.25$, $C_{r_1} = 0.04645$, $C_{r_2} = 0.25$, $\eta = T^2(\mathbf{S}:\mathbf{S} - \mathbf{W}:\mathbf{W})$, $T = \max(T_1, T_3)$ is the near-wall asymptotic behavior time-scale, $T_1 = 1/(\beta^*\omega)$, $T_2 = 6\sqrt{\nu/(\beta^* k\omega)}$, and $T_3 = (T_1^{1.625}T_2)^{1/(1.625+1)}$ are model coefficients, $\mathbf{W} = \mathbf{W}^l + \mathbf{W}^f + (C_{\text{ct}} - 1)\mathbf{W}^S$ is the absolute rotation tensor, $C_{\text{ct}} = 2$ is a model coefficient, $\mathbf{W}^l = \frac{1}{2}\left(\nabla\overline{\mathbf{u}} - \nabla\overline{\mathbf{u}}^T\right)$ is the local frame of reference contribution, $\mathbf{W}^f = \mathbf{E}\cdot\boldsymbol{\omega}^f$ is the rotating frame of reference contribution, $\boldsymbol{\omega}^f$ is the frame rotation vector, $\mathbf{W}^S = \mathbf{W}^f - \mathbf{E}\cdot\left(\mathbf{A}^{-1}\cdot\boldsymbol{\omega}^S\right)$ is the streamline curvature contribution, $\mathbf{E}$ is the Levi-Civita tensor (i.e. third-order permutation tensor),

$\mathbf{A} = \mathbf{I} - 3\mathbf{S}^2/(2\mathbf{S} : \mathbf{S})$, $\boldsymbol{\omega}^S = \mathbf{E} \cdot \left[(\mathbf{S} \cdot (D_t\mathbf{S}) - (D_t\mathbf{S}) \cdot \mathbf{S})/(2\mathbf{S} : \mathbf{S}) \right]$, and $D_t\mathbf{S}$ is the strain-rate tensor total derivative. When curvature correction is not enabled in STAR-CCM+, $f_c = 1$.

$$f_c = \min\left(C_{\max}, \frac{1}{C_{r_1}(|\eta| - \eta) + \sqrt{1 - \min(C_{r_2}, 0.99)}}\right) \tag{41}$$

The VOF model provides an interface-tracking method for immiscible fluids that are assumed to share the same velocity, pressure, and temperature fields. In order to track where each fluid exists in the computational domain, the advection of a phase volume fraction field variable α, which describes the proportion of a fluid in a volume mesh cell, is modeled by an additional transport equation, which takes on the following form, where $\mathbf{a}$ is the surface area vector, $\mathbf{u}$ is the mass-averaged velocity, $\mathbf{u}_{d,i}$ is the diffusion velocity, S_{α_i} is a user-defined source term of phase i, and $D\rho_i/Dt$ is the material derivative of phase i's density.

$$\frac{\partial}{\partial t}\int_V \alpha_i dV + \oint_A \alpha_i \mathbf{v} \cdot d\mathbf{a} = \int_V \left(S_{\alpha_i} - \frac{\alpha_i}{\rho_i}\frac{D\rho_i}{Dt}\right)dV - \int_V \left(\frac{\nabla \cdot (\alpha_i \rho_i \mathbf{u}_{d,i})}{\rho_i}\right)dV \tag{42}$$

The volume fraction must remain in the range of $0 \leq \alpha \leq 1$ with pure air and water phases being represented by $\alpha = 0$ and $\alpha = 1$, respectively, in all simulations generated for this research. The VOF model computes material properties including density and dynamic viscosity in volume mesh cells where the fluid interface exists (i.e. where $0 < \alpha < 1$), as weighted averages as given by the following formulas, where ρ_i and μ_i are the density and dynamic viscosity of phase i.

$$\rho = \sum_i \rho_i \alpha_i \tag{43}$$

$$\mu = \sum_i \mu_i \alpha_i \tag{44}$$

Both water (ρ=997.561 kg m^{-3}, μ = 8.8871E−4 Pa · s) and air (ρ=1.184 15 kg m^{-3}, μ = 1.85508E−5 Pa · s) were assumed to behave as incompressible fluids using their STAR-CCM+ default physical property values. This is a physically-reasonable assumption, since the maximum velocity of air computed in simulations was far below $M = 0.3$, the Mach number at which compressible flow effects become appreciable (Johnson 2016). For example, during wave breaking and onshore impacts, some air phase-dominated cells reached up to 45 m s^{-1} for brief intervals, which is equivalent to $M = 0.13$ at p=1 atm and T=300 K.

Surface tension effects at the water-air interface or free surface were incorporated using a continuum surface force (CSF) model (Brackbill et al. 1992). Surface tension forces act as tensile, cohesive forces tangential to the free surface, which are scaled by a surface tension coefficient defined as a force per unit length (σ=0.072 N m^{-1}) and incorporated as body forces into the Navier-Stokes momentum equations. They are primarily a function of the local free surface curvature, which induces forces normal to the free surface, $\mathbf{f}_{\sigma,n}$, but may also be influenced by temperature changes that cause local variations in the surface tension coefficient, which generate forces tangential to the free surface, $\mathbf{f}_{\sigma,t}$ (Siemens Digital Industries Software 2023c). These forces are summed to give the total surface tension force, $\mathbf{f}_\sigma = \mathbf{f}_{\sigma,n} + \mathbf{f}_{\sigma,t}$. These force components are computed according to the following equations, where $\mathbf{n} = \nabla\alpha_i$ is the unit vector normal to the free surface pointing from water to air, $\mathbf{t}$ is the unit vector tangent to the free surface, $\kappa_\sigma = -\nabla \cdot (\nabla\alpha_i/|\nabla\alpha_i|$ is the mean curvature of the free surface.

$$\mathbf{f}_{\sigma,n} = \sigma\kappa_\sigma\mathbf{n} = -\sigma\nabla \cdot \left(\frac{\nabla\alpha_i}{|\nabla\alpha_i|}\right)\nabla\alpha_i \tag{45}$$

$$\mathbf{f}_{\sigma,n} = \frac{\partial\sigma}{\partial\mathbf{t}}\mathbf{t} \tag{46}$$

Rather than explicitly model the debris objects with a full FSI approach (e.g., utilizing the Solid Stress and 6-DOF Dynamic Fluid-Body Interaction (DFBI) models with an overset mesh), the DEM model, a sub-model of the Lagrangian Multiphase (LMP) model, was employed (Siemens Digital Industries Software 2023d). The DEM model allows for simulations of discrete, solid objects incorporating inter-particle contact forces. Typically, DEM is applied to dense particle flows (e.g., sand/gravel, powders,

capsules, and fibers), which makes it an excellent option for modeling tsunami inundation-driven debris flows. In the case of this research, only a small number of objects (i.e. 3 to 6) was defined, but in practice an entire field of debris could be generated. In addition to fundamental object shapes such as spheres, cylinders, and capsules, polyhedral bodies may be used to define a DEM particle shape, allowing for arbitrarily-shaped objects to be incorporated into a debris flow simulation. The 1:40 scale shipping container-like debris objects used by Goseberg et al. 2016b were modeled in STAR-CCM+ using the polyhedral DEM particle type with a 60 mm x 60 mm x 150 mm sized Block type of Shape Part as the geometry input.

Fluid flow effects acting on the DEM particles were incorporated by enabling the pressure gradient force, drag force, drag torque, and virtual mass models. The dimensionless virtual or added mass coefficient is defined as the ratio of a body's mass to the mass of fluid its volume would displace, which gives 0.226 kg / (997.561 kg m^{-3} x 0.15 m x 0.06 m^2) = 0.4195 as the coefficient value for the debris. Both DEM-DEM particle and DEM-wall boundary interactions were accounted for using the linear spring and rolling resistance models, for which the friction and restitution coefficients were set as 0.45 and 0.5, respectively. All other coefficients for the linear spring and rolling resistance models were left as their default values. Each of these effects are accounted for in the conservation of linear and angular momentum equations defined below, where m_p is the DEM particle mass, $\mathbf{u}_p$ is the particle velocity vector, $\mathbf{F}_s$ is the resultant of surface forces acting on a DEM particle, $\mathbf{F}_b$ is the resultant of body forces acting on a DEM particle, $\mathbf{I}_p$ is the DEM particle moment of inertia tensor, $\boldsymbol{\omega}_p$ is the DEM particle angular velocity, $\mathbf{M}_b$ is the drag torque, and $\mathbf{M}_c$ is the resultant contact force moment.

$$m_p \frac{d\mathbf{u}_p}{dt} = \mathbf{F}_s + \mathbf{F}_b \tag{47}$$

$$\mathbf{I}_p \frac{d\boldsymbol{\omega}_p}{dt} = \mathbf{M}_b + \mathbf{M}_c \tag{48}$$

The resultant surface and body force terms are comprised of the following components, where $\mathbf{F}_d$ is the drag force, $\mathbf{F}_p$ is the pressure gradient force, $\mathbf{F}_{vm}$ is the virtual mass force, $\mathbf{F}_g$ is the gravity force, $\mathbf{F}_{MRF}$ is the moving reference frame-induced force, $\mathbf{F}_u$ is the user-defined body force, $\mathbf{F}_c$ is the contact force, and $\mathbf{F}_{Co}$ is the Coulomb force. No moving reference frame, user-defined body, or Coulomb forces were included in this research, so they have been neglected beyond this point.

$$\mathbf{F}_s = \mathbf{F}_d + \mathbf{F}_p + \mathbf{F}_{vm} \tag{49}$$

$$\mathbf{F}_b = \mathbf{F}_g + \mathbf{F}_{MRF} + \mathbf{F}_u + \mathbf{F}_c + \mathbf{F}_{Co} \tag{50}$$

Each of these force components are computed according to the following equations, where C_d is the drag coefficient, ρ is the continuous phase (i.e. the VOF model fluid in this research) density, A_p is the projected area of the DEM particle, $\mathbf{u}_s = \mathbf{u} - \mathbf{u}_p$ is the DEM particle slip velocity vector, $\mathbf{u}$ is the continuous phase velocity vector, V_p is the DEM particle volume, ∇p_{static} is the continuous phase static pressure, C_{vm} is the virtual mass coefficient.

$$\mathbf{F}_d = \frac{1}{2} C_d \rho A_p |\mathbf{v}_s| \mathbf{v}_s \tag{51}$$

$$\mathbf{F}_p = -V_p \nabla p_{static} \tag{52}$$

$$\mathbf{F}_{vm} = C_{vm} \rho V_p \left(\frac{D\mathbf{u}}{Dt} - \frac{d\mathbf{u}_p}{dt} \right) \tag{53}$$

$$\mathbf{F}_g = m_p \mathbf{g} \tag{54}$$

A wide range of drag coefficient models are available in STAR-CCM+ to apply to DEM particles. For this research, the Haider and Levenspiel Drag Coefficient model was utilized. This model defines the DEM particle drag coefficient in terms of the particle Reynolds number, $Re_p = |\mathbf{u}_s| D_p / \nu$, as follows below, where D_p is the DEM particle diameter, $A = 8.1716 \exp -4.0665\phi$, $B = 0.0964 + 0.5565\phi$, $C = 73.69 \exp -5.0746\phi$, $D = 5.378 \exp 6.2122\phi$, and ϕ is the DEM particle sphericity.

$$C_d = \frac{24}{Re_p}\left(1 + ARe_p^B\right) + \frac{C}{1 + D/Re_p} \tag{55}$$

Similarly, each of the moment components may be defined as shown below, where C_R is the rotational drag coefficient, $\mathbf{\Omega} = \frac{1}{2}\nabla\times\mathbf{u} - \boldsymbol{\omega}_p$ is the relative angular velocity vector of a DEM particle to the continuous phase fluid (i.e. the slip-rotation), $\mathbf{r}_c$ is the position vector from a DEM particle center of gravity to a contact point, $\mathbf{F}_{cm}$ is a contact model force, and $\mathbf{M}_{cm}$ is a rolling resistance model moment.

$$\mathbf{M}_b = \frac{\rho}{2}\left(\frac{D_p}{2}\right)^5 C_R|\mathbf{\Omega}|\mathbf{\Omega} \tag{56}$$

$$\mathbf{M}_c = \sum_{contacts} (\mathbf{r}_c \times \mathbf{F}_{cm} + \mathbf{M}_{cm}) \tag{57}$$

Numerical Schemes

When considering fluid flows, STAR-CCM+ offers both Coupled Flow and Segregated Flow Solvers to solve the governing physics equations, the latter of which was selected for this research. The Coupled Flow Solver, which solves the entire set of governing equations simultaneously, is more robust than the Segregated Flow Solver when considering compressible flows or natural convection, for example. Although, the Coupled Flow Solver requires more memory and the flow being considered in this study is incompressible, so the Segregated Flow Solver was identified as the best option.

The Segregated Flow Solver utilizes a pressure-velocity coupling algorithm that works in a predictor-corrector fashion, where an initial velocity field is computed from the momentum equations, then a pressure correction Poisson equation derived from the continuity and momentum equations is solved for the pressure field, and finally the corrected velocity is computed using the new pressure field. STAR-CCM+ offers two pressure-velocity coupling schemes for its Segregated Flow Solver, the Semi-Implicit Method for Pressure Linked Equations (SIMPLE) and the Pressure-Implicit with Split-Operators (PISO) algorithms. Both SIMPLE and PISO have equal temporal accuracy; although, PISO becomes unstable for large time steps (e.g, CFL > 10), whereas SIMPLE maintains stability for larger time steps, but with a consequence of reduced temporal accuracy for transient simulations (Siemens Digital Industries Software 2023e). PISO may offer an advantage of being more efficient than SIMPLE for small time steps, but SIMPLE was selected instead to maintain stability at larger time steps.

To improve the solution stability while decreasing simulation run time as much as possible, the Adaptive Time-Step model was initially employed. A Courant-Friedrichs-Lewy (CFL) number criterion was defined for this model to ensure that the maximum CFL number was limited to 0.5, which is the recommended value to maintain solution stability and accuracy when utilizing second-order time-stepping with the Segregated Solver flow solver in STAR-CCM+ while running a VOF simulation (Siemens Digital Industries Software 2023f).

However, this CFL criterion led to very long simulation run times. In an effort to speed up simulation runs, larger, fixed-value time step values were tested. It was found that using a time step of 0.001 s reduced run times significantly yet did not change the wave height results appreciably, so this value was used for all simulation run results presented herein. This value was over 10x larger than the mean time step determined by the Adaptive Time-Step model to ensure CFL $\leq$ 0.5 was satisfied at all times, which demonstrates just how restrictive this condition is for VOF free-surface flows.

Alternatively, the Implicit Multi-Step functionality of the VOF solver as well as the Modified High-Resolution Interface Capturing (MHRIC) VOF scheme may be utilized to satisfy these conditions, yet still speed up run times through sub-stepping and relaxing the sharpness of the free-surface interface, respectively. Furthermore, combining these two features with the Adaptive Mesh Refinement and Adaptive Time-Step models would lead to even greater speed-up for VOF simulations. This more robust approach will be the subject of a future research effort aimed at honing in on ideal numerical settings to maintain solution accuracy for tsunami inundation simulations while also reducing run times.

Boundary Conditions

In STAR-CCM+, boundary conditions are applied to Boundaries within a Region. Regions function as collections of geometry, the volume mesh, and a physics continuum, which fully defines the CFD simulation to be solved. All solid boundaries (e.g., the air valve, reservoir, basin, etc... walls) were set

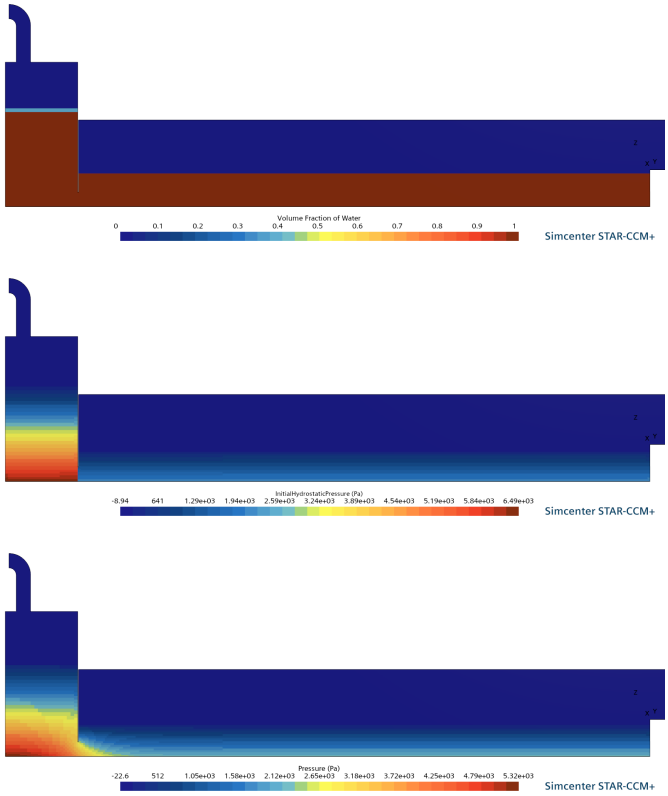

Fig. 3. Side-view of pressure distribution for initial vacuum-chamber release in STAR-CCM+ CFD. (**a**) Initial volume fraction. (**b**) Initial hydrostatic pressure. (**c**) Initial converged pressure.

as the Wall type, which is an impermeable, no-slip condition boundary. Each of the air valve and wave basin openings were set as the Pressure Outlet boundary type. To account for the fact that $p = 0$ kPa was defined as the pressure top of the reservoir (i.e. at $z_{\text{ref}} = 0.745$ m), the pressure at the top of the wave basin was set as $p_{\text{basin atmos}} = -\rho_{\text{Air}}|\mathbf{g}|(z_{\text{basin atmos}} - z_{\text{ref}}) = 4.647$ kPa, where $z_{\text{basin atmos}} = 0.345$ m.

Initial Conditions

Initial water levels in the reservoir and basin were set using the VOF Waves model to define two flat waves. This was achieved by combining their volume fraction field functions in a single user-defined field function that utilized an if-statement to switch between the flat waves depending on the y-coordinate (e.g., the reservoir flat wave was used if $y < -3.95$ m, otherwise the basin flat wave was used). For the initial pressure distribution, a single time-step simulation run was executed with numerous inner iterations to produce a converged initial pressure field. The results were extracted in an XYZ Table and exported to a CSV file to use as the initial condition for full transient simulation runs. The reason this was deemed necessary is that the reservoir opening leads to a non-uniform pressure field surrounding it such that $p = -\rho g(z - z_{\text{ref}})$ is no longer valid near the opening since the pressure field will vary horizontally too due to the sudden change in water depth from the reservoir to the basin. The single-step run, shown in Figure 3 (b), was initialized assuming that a perfect hydrostatic pressure distribution existed in the reservoir and basin by applying the same if-statement approach as was used for the volume fraction in Figure 3 (b) to create a user-defined field function that switched between the hydrostatic pressure field functions of the flat waves. Lastly, the initial fluid velocity throughout the entire simulation region was set to $0.0\,\text{m}\,\text{s}^{-1}$ in all axes directions and the STAR-CCM+ default initial turbulence parameters (i.e. Turbulence Intensity = 0.01, Turbulent Velocity Scale = $1.0\,\text{m}\,\text{s}^{-1}$, and Turbulent Viscosity Ratio = 10.0) were used as well.

To initialize the debris as DEM particles, a table injector utilizing CSV files containing DEM particle

coordinates was created to position sets of debris objects in the simulation region for each debris configuration. To ensure the correct number of DEM particles was generated only during the first time step, a user-defined expression was specified as the particle flow rate value. This expression utilized an if-statement checking the TimeLevel system field function value, where if it is < 1, then the particle flow rate is set as the number of debris divided by the initial time step, but is set as zero otherwise. Additionally, a small gap of 0.0005 m between the vertical stacks of debris and the harbor floor wall boundary was specified in the CSV files, which allowed them to smoothly settle onto one another under the influence of gravity, avoiding the DEM particles propelling themselves away from each other. If DEM particles are initialized touching each other or a wall boundary, then it is highly likely contact or overlap between them will be detected, causing a repulsive force to be generated, the magnitude of which is determined by their elastic properties and the degree of initial overlap.

Volume Mesh Generation

The volume mesh was generated using the Trimmed Cell Mesher with a base size of 0.05 m. Mesh refinement regions were defined using a combination of Surface Controls and Volume Controls. The Target Size values for these controls were set as percentages of the Base Size, namely 25% near the free surface, 50% in the reservoir and near the basin bed, and 20% in the air valve pipes and surrounding the obstacles. Mesh Alignment was enabled for the Trimmed Cell Mesher so that the free surface in the basin was exactly lined up with a horizontal plane of volume mesh cell faces, avoiding intermediate volume fraction values (i.e. in the range $0 < \alpha < 1$ rather than exactly 0 or 1) existing within the basin at the beginning of simulation runs. To account for boundary layer effects, the Prism Layer Mesher was used to generate a 5 cell-thick boundary layer mesh along all Wall type boundaries with a total thickness equivalent to 33% of the local surface mesh sizes. The resulting volume mesh consisted of approximately 6.35 million cells, with varying values for different cases due to the changing number of obstacles.

Parallel Scaling and Hardware Used

All simulations were run on the same HPC cluster using either 5 or 10 compute nodes per job, where each node has 40 physical cores. Each compute node of the cluster consists of pairs of Intel Xeon Gold 6248 CPU @ 2.50 GHz processors, which have 20 physical cores each with 2 threads per core and 192 GB RAM, connected by Dell PowerEdge C6420 server hardware. Initial test runs were executed using 200 cores over 5 nodes per run, but the final results presented here were completed using 400 cores over 10 nodes per run in order to significantly reduce the run time. Comparing compute times for 12.0 s of simulated time showed that runs completed in roughly 10.25 h and 6.5 h of physical time for 200- and 400-core jobs, respectively.

5 COMPARISON OF WAVE AND DEBRIS DYNAMICS

This section compares the numerical results in ClaymoreUW MPM, DualSPHysics SPH, and STAR-CCM+ CFD relative to the experiments presented in Goseberg et al. 2016b. We segment the comparison along five categories of special interest for tsunami debris modeling: **(i)** Hydrodynamics, **(ii)** Debris Longitudinal Displacement, **(iii)** Debris Lateral Spreading Angle, **(iv)** Debris Motion, and **(v)** Debris Accelerations / Obstacle Loads.

5.1 Hydrodynamics

The first-step in validation of numerical flume results is the validation of a method's capability in resolving the wave-form throughout the flume's length. Elevation results for the four wave gauges along the flume as specified in Table 1 are shown in Figure 4 and discussed below. To start, a description of the experimental wave relative to each wave gauge is given.

The goal of the wave-maker configuration is to generate "wave-trains" as the model for an "irregular" tsunami wave prototype, and thus the wave is designed to have a front which is approximated as a steepened solitary wave while the tail elongates to replicate the long inundation timescale of the prototype tsunamis. Of course, Waseda University's Tsunami Wave Basin facility can't achieve an ideal model timescale of a tsunami wave relative to its amplitude, as these may last hours. We are mostly interested in the initial wave impact and the debris dynamics, so wave events which scale up-to 10 – 30 s prototypes are reasonable for this comparative experimental-numerical study, but they may limit extrapolation of results to prototype tsunami events; the implications have been thoroughly discussed in tsunami-related literature (Madsen et al. 2008; Goseberg et al. 2013).

Wave gauge 1 (WG1) is placed near the wave-maker to capture the initial fluid elevation surge from the pressurized reservoir and the elongated tail before the wave has moved near the harbor apron. Wave gauge 2 (WG2) is located over the water basin but nearer to the harbor quay wall. We observe a slightly increased wave-peak, which tapers off due to the elongated wave-form. Half a second after, reflected waves from the quay wall begin to dominate elevation. Wave gauge 3 (WG3) is above the initially dry harbor apron and positioned prior to the initial upstream debris positions. Replicating the waves measurements is essential to initial mobilization of debris against friction corresponding vertically stacked debris. Wave gauge 4 (WG4) is past the upstream debris and both of the obstacle rows, but prior to the downstream debris position. Accuracy in wave-depth and flow-speed here is vital to drive upstream debris displacement and lateral spreading through the port setting. This gauge ascertains if a method can create a persisting, thin flow over the dry horizontal harbor.

With the anticipated observations at each wave gauge described, we now refer to Figure 4 to compare numerical replications against experimental readings.

MPM is seen to perform respectably in initial hydrodynamic replication in Figure 4, quantified by initial peaks at WG1, WG2, and WG4 constrained within 0.3 cm to 1.8 cm of deviation for grid-cells of 1.0 cm. The sharp peak of WG3 is reduced 6.0 cm, signalling damping in MPM. However, as the discrepancy lasts for 0.05 s the total difference in flow volume is minimal. These results are unexpectedly positive, as the MPM implementation lacks a turbulence model. Interestingly, MPM's laminar flow introduced an initial outflow damping that resembles the brief reservoir pressure release lag our group suspects elongated the wave during the experiments of Goseberg et al. 2016b, though not documented. However, MPM does not elongate the wave at WG1 into a full plateau from 1.0 s to 1.5 s, as seen in experiments. When the wave reaches WG2 it no longer appears to have a shortened timescale, so this may not be a significant error. At both WG3 and WG4, MPM characterizes thin flows with good accuracy in depth, timescales, and arrival times, demonstrating that an ideal elongated tail at WG1 and WG2 is not required to attain the critical elongated thin flow on the harbor for studying debris. However, flow at WG3 and WG4 are typically 0.2 cm to 1.0 cm lower than in experiments and the frequency content is damped.

SPH broadly improved matching of the wave-form at all wave gauges compared to MPM, with a trend of decreasing accuracy for increasing elapsed time. Both the inundation at WG3 for a time greater than 3 s, and the thin flow at WG4 appear to be up-to approximately 150% the experimental depth. The SPH team assumes that the mismatch is due to deviations of physically and numerically generated wave signal and experimental conditions. At WG1, the tail of the wave train is mismatched for $t = 1.75$ s to $t = 2.25$ s, indicating a mismatch of water retaining. Additionally, the third wave crest at WG2, originating from the quay wall reflected wave, is of lower magnitude than in the physical experiment, indicating a greater amount of quay wall reflected water. Lower amounts of retained water and reduced wave reflection might therefore contribute to a lower onshore inundation, ultimately leading to a greater accordance of physical experiment and numerical simulation. Furthermore, while the numerical boundary interaction is achieved through the MDBC (English et al. 2022), the boundary velocity is only set to a value of zero and therefore no thorough no-slip boundary condition and therefore accurate near wall-behavior is achieved. In the future, use of wall functions might further increase the accuracy of fluid-wall interaction. Especially the overall temporal evolution of the water surface elevation is reproduced, while not always modelled accurately in magnitude. The accurate reproduction of the water surface elevation is partially due to the iterative fitting process of the vertical acceleration source based on the data at WG1. However, data from WG2 to WG4 show that once the wave generation signal is accurately modeled, the wave transformation is also accurately reproduced within the numerical toolbox.

STAR-CCM+ replicated primary hydrodynamic aspects of interest better than MPM, but it did not match the exact free-surface reading as closely as SPH. However, STAR-CCM+ did not rely on a subjective forcing function in the reservoir to achieve its results, as done in SPH. Instead, a parametric study was performed on simple quantities that were either omitted from Goseberg et al. 2016b (e.g., the outflow gate height) or which may have been experimentally unavailable (e.g., the reservoir pressure decay rate). Variables were examined within plausible rational ranges, including still-water depths, pressure dissipation rates, outflow sluice gate opening heights, etc. to study the first-principals driving the flume's hydrodynamics. As a consequence, no one result is representative of the study or the method's CFD capabilities. However, the submitted wave gauge data attained similar behavior to SPH without using a

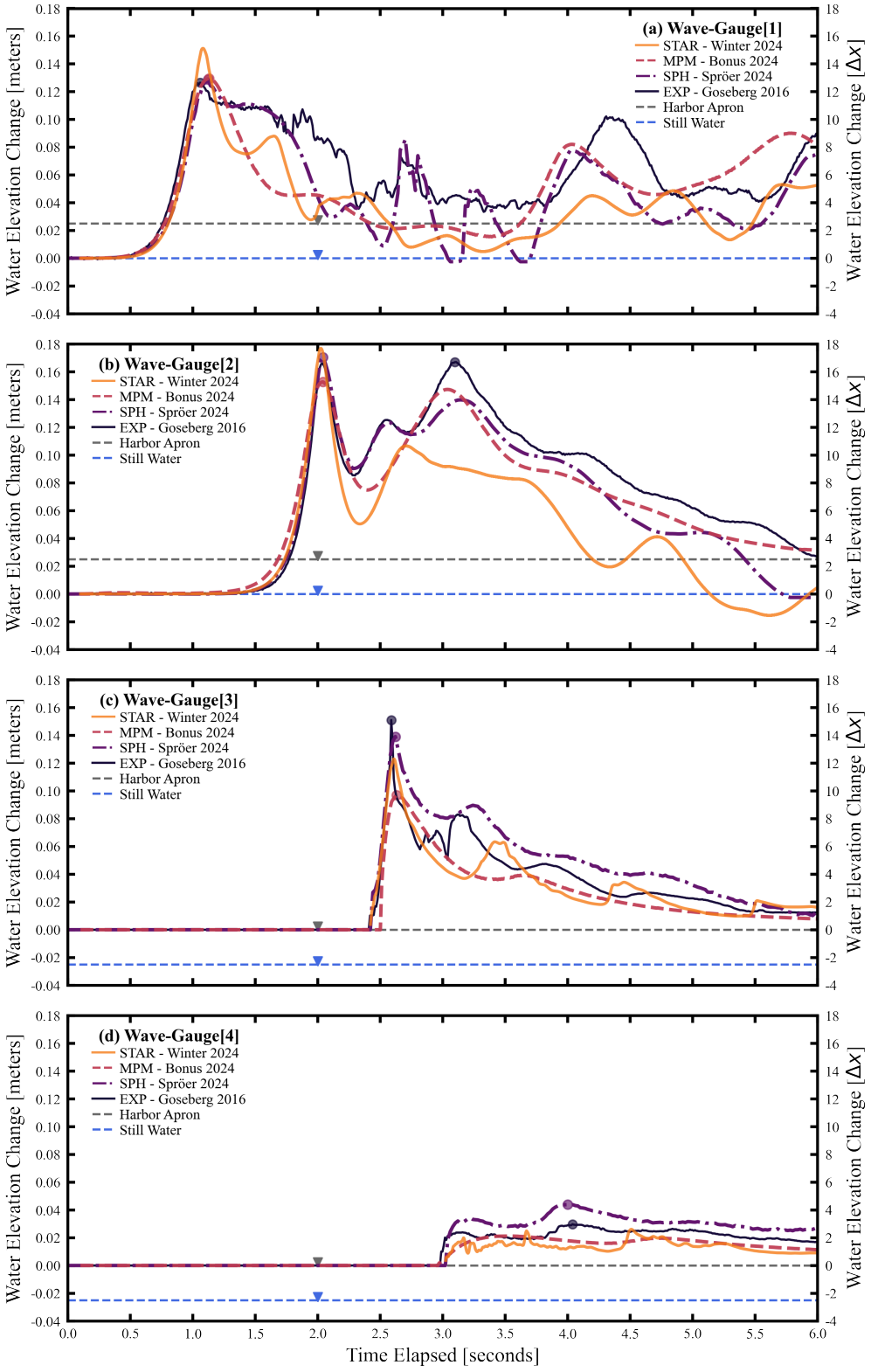

Fig. 4. Free-surface elevation of numerical methods and experiments at four wave gauges in Waseda University's tsunami wave basin. Based on experiments by Goseberg et al. 2016b. Compares ClaymoreUW MPM, DualSPHysics SPH, Siemens STAR-CCM+ CFD, and the experimental ground-truth at four wave gauges.

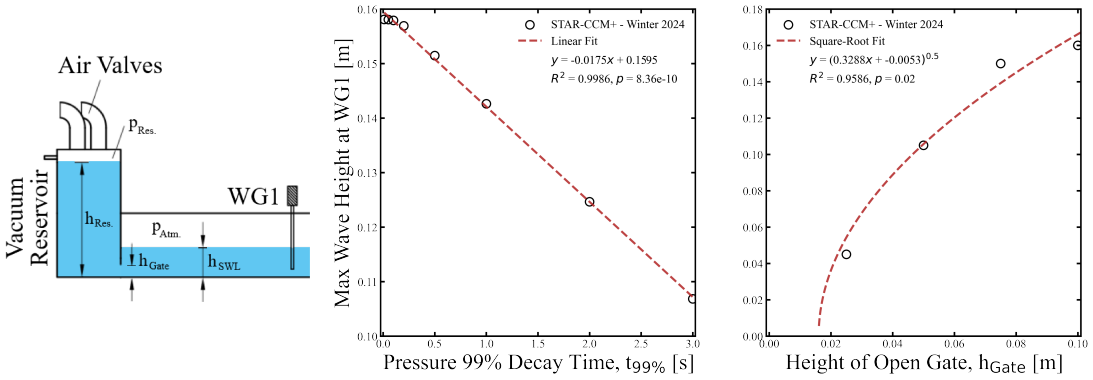

Fig. 5. Influence of the vacuum reservoir's exponential pressure decay and outflow sluice gate height on measured wave amplitude. STAR-CCM+ CFD performs a parametric study on two uncertain variables. **(Left)** Side-view diagram of the wave-flume vacuum-chamber reservoir and water basin prior to the first wave gauge (WG1). **(Center)** Air valve pressure decay. **(Right)** Influence of air valve initial pressure exponential decay duration on WG1 max wave height. Results from STAR-CCM+ demonstrate that even if 90% of the pressure differential in the reservoir dissipates in a second, the influence on measured wave amplitudes and timescales is substantial.

subjective acceleration adjustment. Instead, STAR-CCM+ only modified the initial reservoir fill elevation of 0.90 m to be the supposed pressure head of 0.67 m from Goseberg et al. 2016b while keeping SWL at 0.23 m and outflow gate height at 0.10 m. A typo may have confused the values in the original article, but we emphasize this is not guaranteed, it is only uncertain. Regardless, this is one of the potential facility permutations identified with STAR-CCM+ as plausible sources for the unusual reservoir outflow rate in Goseberg et al. 2016b.

The STAR-CCM+ CFD study on the influence of an exponential pressure decay function on the wave amplitude is provided in Figure 5. Results from STAR-CCM+ demonstrate that even if 99% of the pressure differential in the reservoir dissipates in under a second, the influence on measured wave amplitudes (notably at the first wave gauge) and timescales (drastically altering elongation of the wave following the peak) is substantial. The trend in wave amplitude is linear with changing exponential pressure decay time ($t_{99\%}$). A square-root trend is seen respective to the outflow sluice gate height (h_{gate}) on the right-side plot of Figure 5. Magnitudes of fitted equations on both parameters, and their associated R^2 and p-values, suggest that either uncertain variable, or a combination of the two, may be responsible for the reservoir outflow from Goseberg et al. 2016b.

We note that MPM has quicker decay following the elongated vacuum-chamber waves front when compared to experiments (which may dissipate reservoir pressure more slowly than originally believed), SPH results (which applied an empirically fitted acceleration forcing function to the reservoir to mimic pressure decay), and STAR-CCM+ (which investigated many permutations of the facility to identify the source of the outflow behavior beyond the parameters listed in Goseberg et al. 2016b). This signals that MPM did not elongate the far-field wave as effectively as the other methods, which poses difficulties for tsunami studies (Madsen et al. 2008). However, as the wave progressed onto the harbor the flow did not seem to be notably affected, possessing similar flow depths and duration to the experiments and alternative methods.

Overall, STAR-CCM+ CFD was the only method that readily applied advanced boundary conditions (e.g., modeling individual pressure release valves in the reservoir) to attain plausible, first-principals based hydrodynamics inline with experiments. While MPM fared respectably, despite not using any empirical tuning of the pressurized reservoir flow, it may have relied on the method's inherent damping to mimic the pressure dissipation and turbulence of experiments. SPH best matched the free-surface elevation curves, but did so by applying an empirically tuned acceleration forcing function to the pressurized reservoir. While it replicated the experiments very well, it lacks underlying physical justification and exposes the digital twin to over-fitting, which may bias the results.

For these reasons, we consider STAR-CCM+ to have the best first-principals hydrodynamic capabilities. SPH is also viewed highly, however the use of a non-physical acceleration adjustment is not disregarded, but should be replaced by a more physically justifiable method in the future. Likewise, use of a fluid bulk modulus more comparable to real water should be sought after. MPM is viewed to have performed surprisingly well, albeit with noted damping from its low-order implementation and the full stiffness fluid bulk modulus. However, MPM's lack of a turbulence model suggests studies focused purely on fluid-flow would be wise to select an alternative.

From an experimental point of view, the difficulties in replicating the source of the tsunami-like wave gives rise to future foci on providing more accurate, and more detailed description of the wave generation mechanisms steering the wave energy input in experiments.All modeling efforts took liberties in their approach, and uncertainties in certain flume facility specifications still persist. Physical phenomena such as air entrainment (Iafrati 2011), experimental inaccuracies such as possible water leakage at gaps in wooden plates of the physical harbor apron, and the initial dampness of the harbor apron are also not considered fully, but might contribute to free surface deformation (Ghodoosipour et al. 2019).

5.2 Longitudinal Displacement

In this section, we assess numerical methods in replication of onshore distance traveled by wave-driven large debris mobilized through varied obstacle arrays. This is to check if said methods capture the influence of obstacle configuration on longitudinal debris displacement, as observed in Goseberg et al. 2016b.

Longitudinal displacement of adjacent and stacked shipping containers in harbor ports was observed during the Tohoku 2011 tsunami. These large debris have simple geometries, pose significant hazards, begin in predictable arrangements of stacked side-by-side placement (von Häfen et al. 2021), and are uniquely identified by serial numbers and thus allowed researchers to estimate the motion of each debris during inundation (Naito et al. 2014). Here, we consider an experimentally fitted predictive model for longitudinal displacement from Nistor et al. 2017a, defined as

$$\Delta_{\text{Long.}} = (3.58 - 0.09 N_{\text{Debris}}) \text{ meters} , \tag{58}$$

where N_{Debris} is the number of debris in the trial. This is a reasonable prediction on median longitudinal displacement, based solely on the number of debris and trends observed in the Waseda University flume. Note the constant of 3.58 m only makes sense for the harbor length in the Waseda flume, this equation is not for prototype tsunami design. The negative linear trend with debris count N_{Debris} does imply a more general tendency for larger groups of debris to aggregate and dissipate momentum in a way counterproductive to longitudinal displacement, which is a simple but limited litmus test for any numerical replications as the zero, one, and two obstacle row cases should have median longitudinal displacement in descending order.

Trends in longitudinal displacement of debris, if further developed relative to debris and obstacle configurations, may allow for a back-calculation of the forward longitudinal displacement when given only the drawdown resting position. This has notable value for post-tsunami reconnaissance as perishable drawdown resting positions for debris can be recorded in order to later retrieve critical, yet hard to determine, forward inundation positions. Their criticality is based on both the forward longitudinal displacement of debris establishing the starting point of potentially hazardous debris drawdown paths, and because these measures allow inference of site-specific cutoffs for exposure to debris hazards relative to a structure's distance from the shoreline.

Figure 6 displays all numerical results, experimental trials, and the fitted predictive equation considered for debris longitudinal displacement. It is segmented by the number of obstacle rows and the starting position of the debris-field. All individual experimental and numerical trials are included as points for completeness at the individual debris granularity. Note that both upstream and downstream debris cases were examined numerically for 6-debris configurations across all methods in Figure 6. Optional 3-debris configurations for upstream cases were provided for SPH. STAR-CCM+ includes the 3-debris upstream case without obstacles. MPM does not include the optional 3-debris variant in any case.

A fitted prediction from the experiments of Nistor et al. 2017b, Equation 58, is superimposed on Figure 6 to provide a general guideline for typical debris motion behavior without obstacles that exists outside Goseberg et al. 2016b. Said predictive model shows that the experiments of Goseberg et al.

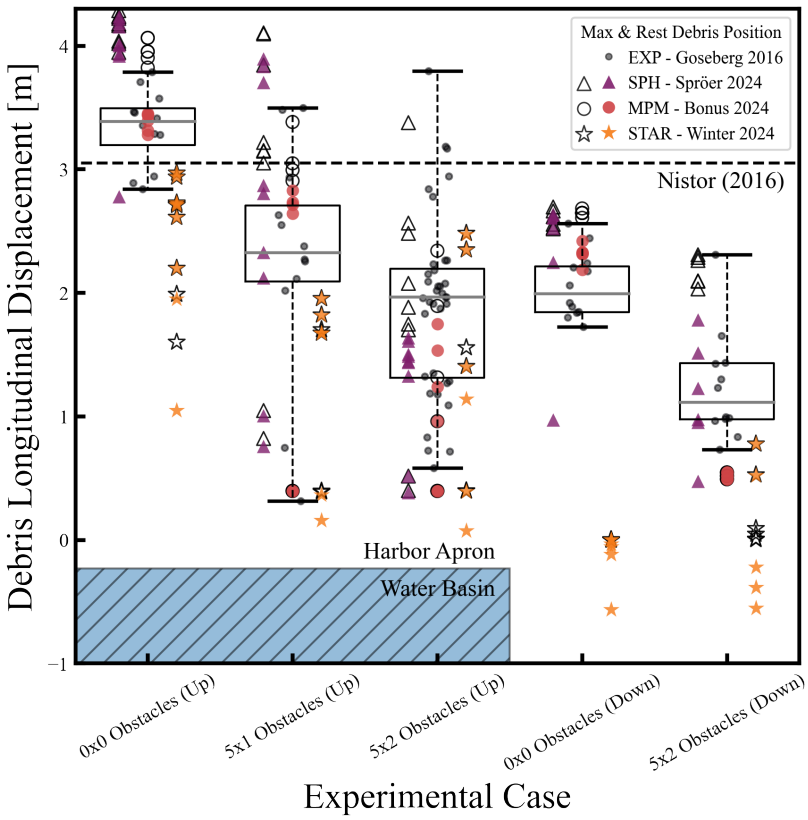

Fig. 6. Debris longitudinal displacement in numerical methods plotted against experiments and empirical predictions. Individual debris results segregated by case for the numerical methods are plotted relative to experiments by Goseberg et al. 2016b. "Up" and "Down" denote the initial debris positions as upstream or downstream (see Goseberg et al. 2016b). All methods include 6-debris results, with SPH providing additional 3-debris results for upstream cases, STAR-CCM+ providing the 3-debris 0x0 obstacles upstream case, and MPM not including the variant in any instance. Black whisker caps are minimum and maximum experimental data-points. The boxes' gray interior line is the experimental median and the top and bottom of said box are the first and third experimental quartile. The predictive equation from Nistor et al. 2017b is included as a dashed line. A blue hatched box is shown below cases with upstream debris to illustrate debris proximity to the water basin and quay wall.

2016b measure similar longitudinal displacement for debris (percent error of 12%) in the upstream configuration without obstacles, but feature less displacement as rows of obstacles are introduced and when the downstream debris configuration is applied. This is because neither aspect was considered in Nistor et al. 2017b, so its applicability herein has limitations. Because the the highest allowed longitudinal displacement is the back wall of the flume, all cases have an absolute upper bound.

Simulation snapshots of a six-debris MPM case with two rows of obstacles are presented in Figure 7. Notably, centerline debris dam at the first obstacle while exterior debris travel past it along the inter-column jet-streams. Rest positions are within experimental distributions from Goseberg et al. 2016b.

SPH results for the six-debris case with two rows of obstacles are shown as simulation snapshots in Figure 8. Debris in SPH move approximately 20% further forward during run up inundation than in MPM but remain within reasonable expectations of experiments. During drawdown, SPH results show a consistent trend of moderate longitudinal displacement towards the basin. The exception is for the zero obstacle cases where the debris get very close to the flume's back-wall during run up, which leads to longitudinal debris motion arrest as they submerge in the reflecting fluid volume by the back-wall.

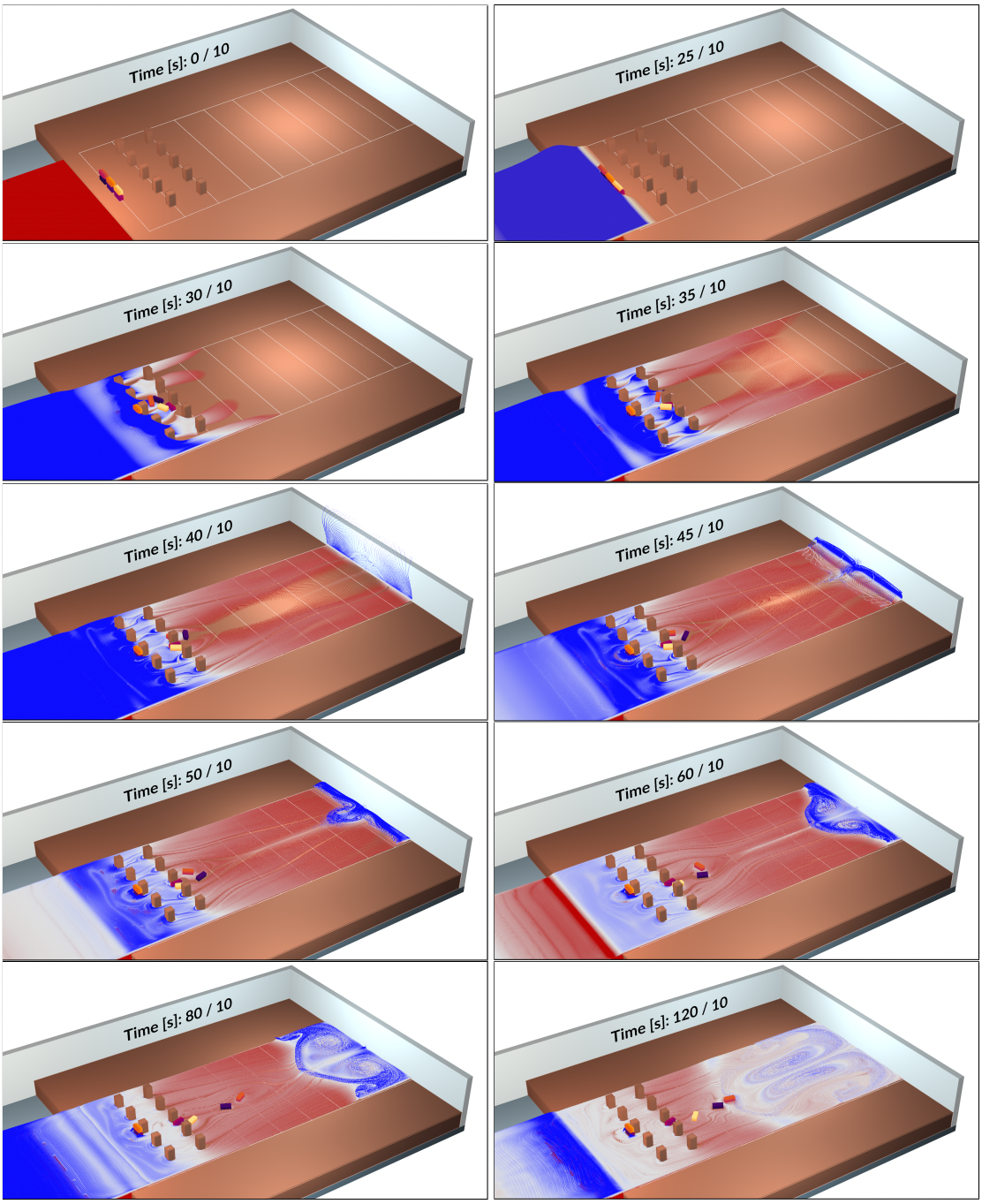

Fig. 7. Wave-driven motion of six debris through two rows of obstacles in MPM. ClaymoreUW MPM simulation of one layer of three 1:40 Froude scaled shipping container debris displacing under inundation while resting on an initially dry, frictional harbor. Two rows of five column obstacles are present in the simulation. Final resting positions lay within the experimental distribution (no outliers). 0.5 mincrements shown as white transverse lines. ID number is colored uniquely per debris, elevation is visualized on the water.

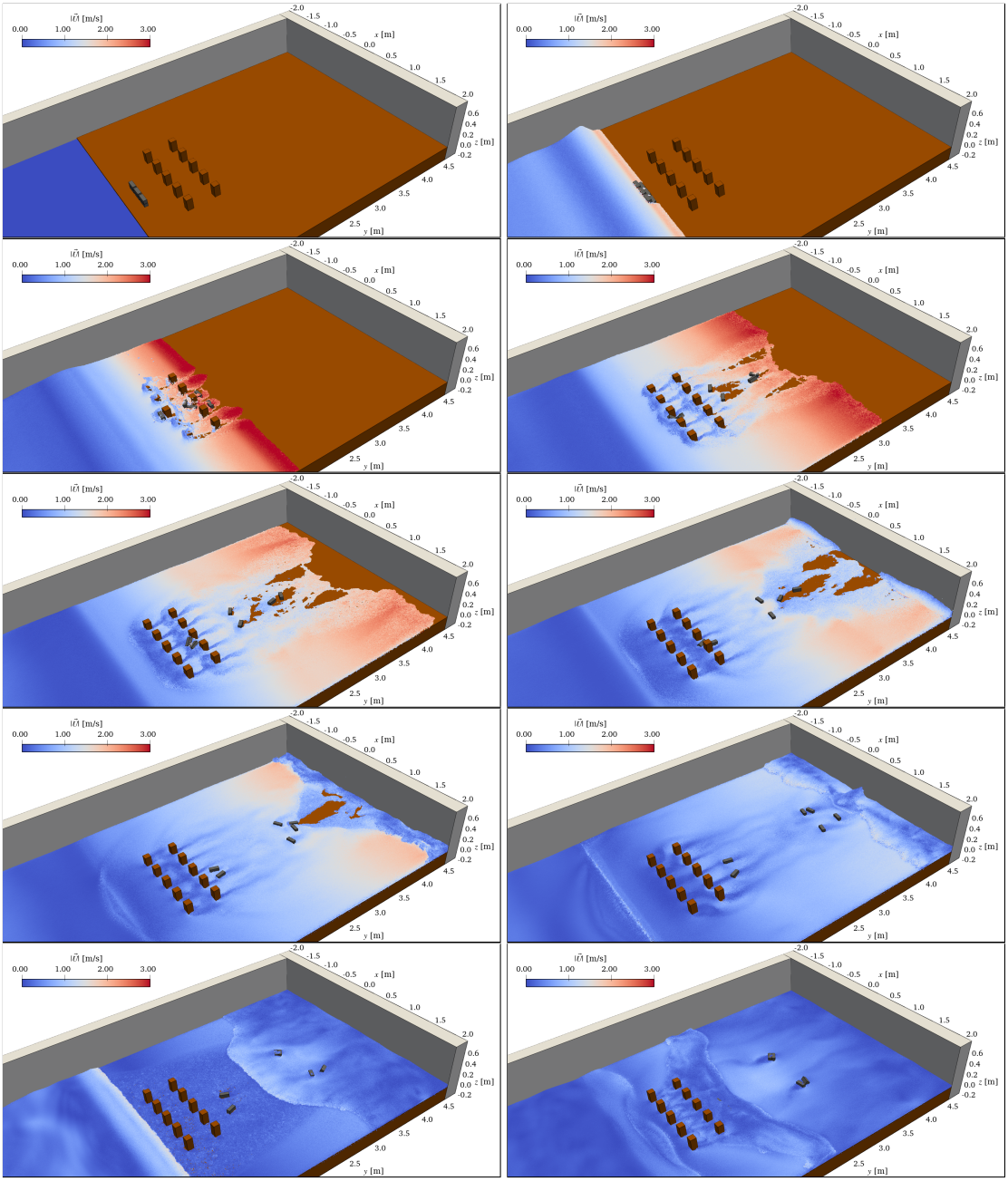

Fig. 8. Motion of six vertically stacked debris across a frictional harbor in SPH. DualSPHysics simulation of six debris arranged in two vertical layers of three 1:40 Froude scaled shipping container debris displacing under inundation while resting on an initially dry, frictional harbor. Two rows of five uniformly spaced square columns (5x2 obstacles, transverse and parallel to flow, respectively) are placed streamwise to constrain the inundating flow and debris motion. Velocity visualized on water particles, with blue, white, and red mapping to 0.0, 1.5, and 3.0 $\mathrm{m\,s^{-1}}$.

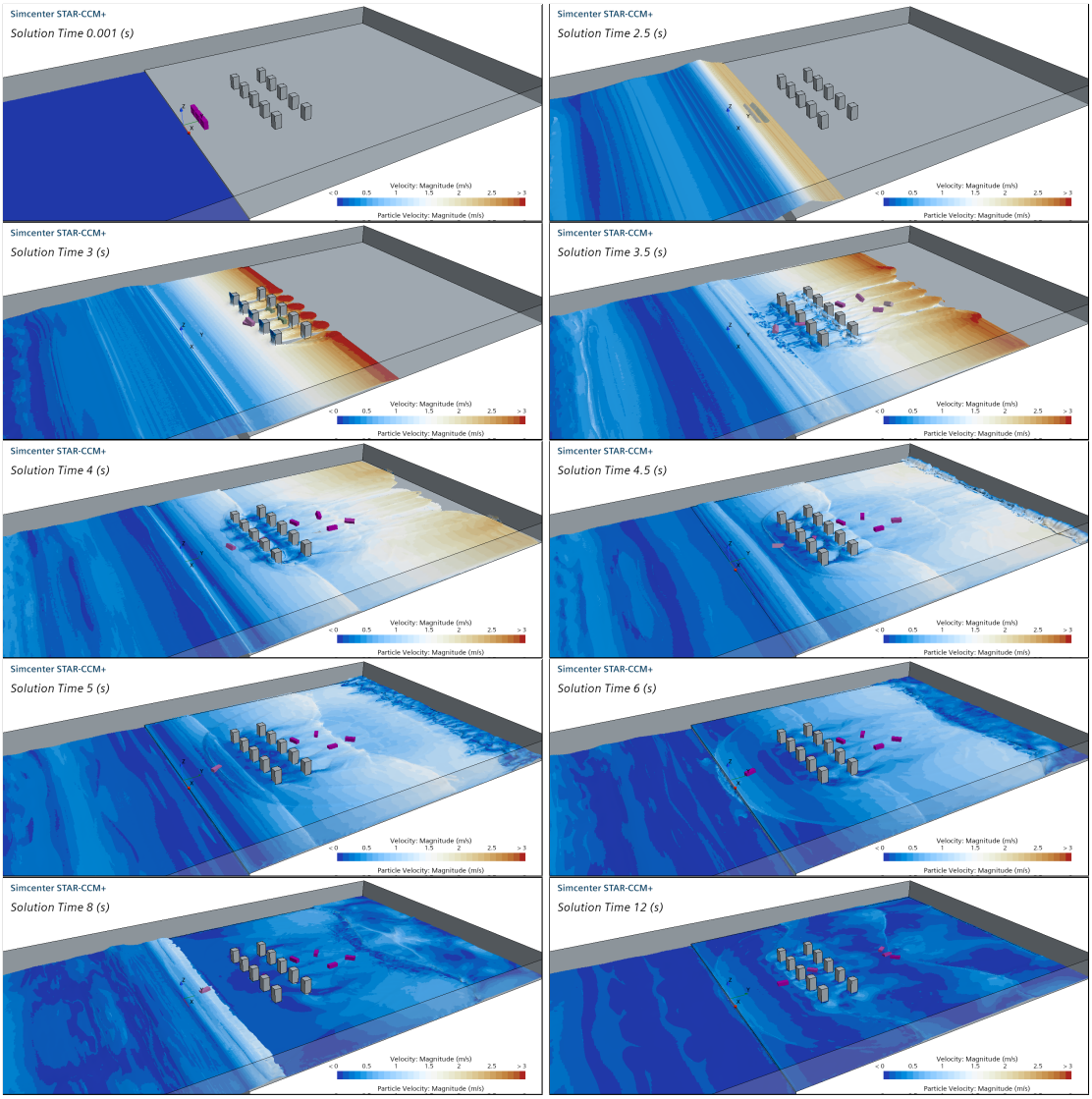

Fig. 9. Wave-driven motion of six debris through two rows of obstacles in STAR-CCM+ CFD. STAR-CCM+ CFD simulation of six debris arranged in two layers of three 1:40 Froude scaled shipping container debris displacing under inundation while resting on an initially dry, frictional harbor. Two rows of five column obstacles (5x2 configuration) are present in the simulation. Velocity visualized on the water.

STAR-CCM+ simulation snapshots are presented in Figure 9 for the 6-debris upstream case with a 5x2 obstacle configuration. STAR-CCM+ CFD exhibits a flow-field similar to that of SPH, which is apparent in the replication of an approximately straight borefront with only small flow gaps behind obstacles at time t = 3.0 s as observed for SPH in Figure 8. This is unlike MPM, which showed a far greater impedance of the inundating flow as it passed obstacles and mobilized debris in Figure 7, as the bore front was notably disturbed by time t = 3.0 s.

MPM simulations capture forward and drawdown longitudinal displacement with good accuracy in nearly all evaluated cases. MPM debris are almost all within the experimental envelopes of Goseberg et al. 2016b, except a fully dammed debris in the upstream 5x2 obstacle case and the under-prediction for all debris in the downstream 5x2 obstacle case. MPM more consistently falls within the interquartile range than in SPH. However, MPM is less likely to characterize the displacement distributions extrema,

which may suggest slight damping in the numerical method.

Both MPM and SPH show similar behavior for the relative longitudinal displacement occurring between the forward inundation and drawdown rest position of debris, except for the no-obstacles case where SPH shows only minimal drawdown displacement while MPM shows notable retreat despite both methods reaching a similar max longitudinal displacement during forward inundation.

STAR-CCM+ CFD simulations generally show an underestimation of longitudinal displacement in Figure 6. They mainly fall within the experimental range for the upstream 5x1 and 5x2 obstacle cases, but systemically fall short in the other cases. This is believed to be a consequence of the STAR-CCM+ approach raising the effective draft depth of debris from an estimated 2.0 – 2.5 cm to 3.0 cm (i.e., at the debris' centroid). This is significant, as the flow-depth itself oscillates between 1.75 cm to 3.5 cm over the harbor. A more advanced debris-fluid coupling approach, of which multiple are available within STAR-CCM+, may resolve this issue, but is not studied herein.

In summary, MPM has the edge in longitudinal displacement over SPH and STAR-CCM+, but all performed well. MPM placed more debris within the experimental distributions' interquartile range. STAR-CCM+ showed its best results when flow-depths were heightened (e.g., due to presence of additional obstacles and for the upstream cases), as the artificially increased debris draft reduced displacement in for low flow-depths. This is seen in the 0x0 obstacle downstream debris case in Figure 6, where STAR-CCM+ debris do not displace forward in the thin run up flow but displace backwards in the deeper, reflected drawdown wave. SPH showed its strength in reasonable characterization of every experimental case, and it was able to capture the extrema of the distributions, albeit with an increased risk of exceeding the experimental envelopes as outliers.

We reiterate that the latter observation may be due to the lower friction coefficients applied by the SPH team than that of the MPM modelers, or due to the differences in the mathematical representation of friction at boundaries in either method. As the exact coefficient for the wetted wood flooring against the HDPE debris is not known, and likely grain dependent (i.e., longitudinal is not equivalent to lateral), we can not confidently determine what coefficient is appropriate. As longitudinal displacement of debris in thin-flows is highly affected by the friction coefficients, the implementation of the friction model, and the amount of hydrodynamic drag and buoyancy the debris experiences in a flow, comparability is not straightforward. We further note that future benchmark cases should always include testing of dry, wetted and other frictional coefficients, both for debris-debris, and debris-boundary interaction, fostering numerical simulation efforts.

5.3 Lateral Spreading Angle

Lateral spreading angle is a significant variable for tsunami debris design. The increase in spreading angle has a linear relationship with the potential spreading area (for a fixed longitudinal displacement) and thereby causes a proportional increase in the inventory of structures at risk of debris-field impact. However, radiating spread from an initial debris-field centroid, such as for a collection of shipping containers, can reduce the total density of debris along the advancing front's arc-length (assuming that debris do not form strong aggregates, which may occur). This means the probability of damming and impact loads on an individual building are expected to decrease along some other proportionality relationship to lateral spread. The commonly used conservative guideline from Naito et al. 2014 suggests flat spreading angles of 22.5°, which are often applied in both forward and drawdown inundations. It is of special interest to quantify the influence of topography, flow characteristics, debris geometry, and infrastructure arrangement (e.g., marginal effect of each added row of structures) on debris-field lateral spreading angle.

In flume experiments of Goseberg et al. 2016b, added rows of obstacles tightened interquartile ranges for spreading angle but increased points exceeding the 95% confidence interval, i.e., outlier events became more likely and the risk of a large group of debris contacting an individual structure within the tight spreading path was increased.

This effect is probably due to **(i)** flow through obstacle gaps becoming channelized and thus altering debris linear and angular velocity and **(ii)** increased likelihood of obstacle impact means kinetic energy of debris redirects transversely more frequently. The second contributor is seen, in wave flumes, to decrease longitudinal displacement, which equates to a decrease of inland infrastructure exposed to debris impacts and damming. However, we emphasize that this is dependent on the tsunami wave's timescale, as longer

lasting flows may re-mobilize debris that lose momentum from impacts. Although an elongated vacuum-chamber wave is applied, the timescale studied and in nearly all wave flumes without pumps will have shorter inundation timescales than a significant tsunami event. This suggests that decrease in longitudinal displacement due to obstacles is probably less apparent at prototype scales, but the lateral spreading angle is as apparent or greater for long timescale inundation.

Predictions from Naito et al. 2014 which apply to conservative design for the spreading of large shipping container like debris in tsunamis and Nistor et al. 2017b are plotted in Figure 10 as interval bounds. We anticipate the former to very rarely be exceeded (it is conservative) while the latter may feature the occasional transgression. It is of special interest to see how obstacles in each numerical method affect the spreading of debris, as impacts and weaving motion through the columns could lead to debris simulations with large lateral spreads or dammed formations between columns if errors are present. As in Nistor et al. 2017b, lateral spreading angle may be defined as the trigonometric relationship between longitudinal and lateral displacement, which is then fitted with regression coefficients for similar Waseda University flume experiments as

$$\pm\theta_{\text{Spread}} = \arctan\left(\frac{\Delta_{\text{Lat.}}}{\Delta_{\text{Long.}}}\right) = \pm 3.69^{\circ} \pm 0.80^{\circ} N_{\text{Debris}} \ , \tag{59}$$

which forms a more reasonable bound on lateral spreading compared to the over-conservative guidelines of Naito et al. 2014, although this is very specific to the Waseda flume experiments.

Figure 10 displays statistical data for debris lateral displacement across experimental cases as a box-and-whisker plot. SPH and MPM appear to capture the general lateral spread of experiments by Goseberg et al. 2016b, Stolle et al. 2016, and Nistor et al. 2017b. SPH shows a tendency towards characterizing the extents of the spread, with two and one debris exceeding experimental envelopes in the single row and double row of obstacles cases. MPM favors more modest but still reasonable spreading values as it never exceeds the guideline suggested by Nistor et al. 2017b, whereas SPH does so multiple times and even crosses the conservative guideline of Naito et al. 2014 twice. However, this is primarily during drawdown spreading, which can be measured relative to initial position or max run up position, so it may be a side-effect of our application of the former definition. Akin to MPM, STAR-CCM+ CFD shows more moderate spreading angles for the cases of debris in front of the obstacles (upstream). However, for the debris positioned behind the obstacles (downstream), the debris also cross the conservative guideline of Naito et al. 2014 twice, though only one is visible in Figure 10. One data-point is omitted from STAR-CCM+ results due to insufficient displacement, disallowing meaningful spreading angle computation. Generally, STAR-CCM+ characterizes the full experimental distributions well.

STAR-CCM+ CFD captures both the lateral spread of the experimental distributions while typically remaining within the conservative bounds of Naito et al. 2014. STAR-CCM+ results do not appear to have a strong inclination towards concave or convex spreading patterns. While both SPH and MPM have reasonable spreading angles in terms of magnitude across all cases, SPH standouts as the preferred choice. While not evident from Figure 10 alone, the lateral spread of SPH and MPM are broadly "convex" and "concave", respectively meaning "radiates outwards" and "radiates inwards". As the experiments tended to portray the former effect (Goseberg et al. 2016b), it can be said that MPM misrepresents a fundamental mode of the lateral spreading hazard, although this may be specific to the tested obstacle and debris configuration and not a broad deficit, and STAR-CCM+ may not exhibit it fully. Further discussion of this finding is to now be contextualized in the overall motion paths of the tsunami debris.

5.4 Debris Motion Through a Scaled City

Motion of a few large debris due to a driving inundation wave in a scaled port setting is a primary focus of our comparative analysis of numerical tools. Distinct phases of motion should be observed, with particular emphasis on effects of added rows of obstacles, friction coefficients, and debris models. Phases are interpreted as:

- **Motion begins:** Debris overcome static friction with the floor.
- **Collapsing stacks:** Debris in vertical stacks may decouple if relative accelerations exceed debris-debris interface friction and restoring gravity forces.
- **Obstacle collision:** Debris rapidly decelerate at impact with obstacles. Debris nay bounce transversely and can lose some energy to bending of the hollow HDPE debris.

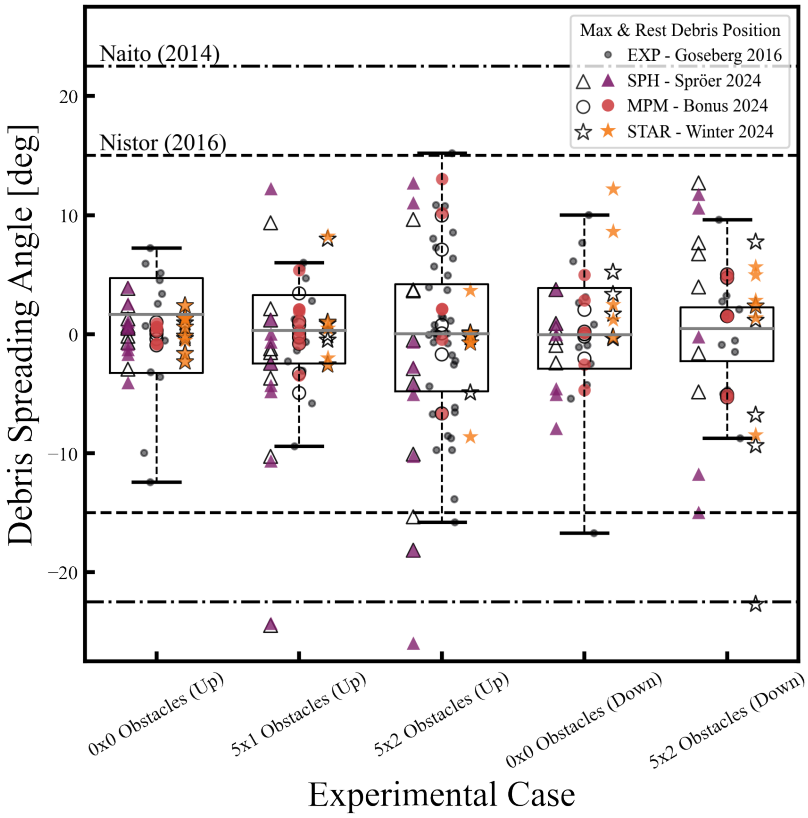

Fig. 10. Debris lateral spreading angles in numerical methods, experiments, and empirical predictions. Individual debris results segregated by case for the numerical methods are plotted relative to experiment by Goseberg et al. 2016b. "Up" and "Down" denote the initial debris positions as upstream or downstream (see Goseberg et al. 2016b). All methods include 6-debris results, with SPH providing additional 3-debris results for upstream cases, STAR-CCM+ providing the 3-debris 0x0 obstacles upstream case, and MPM not including the variant in any instance. Black whisker caps are minimum and maximum experimental data-points. The boxes' gray interior line is the experimental median and the top and bottom of said box are the first and third quartile. Predictive equations from Naito et al. 2014 (conservative) and Nistor et al. 2017b are included.

- **Channel flow:** Passing between adjacent obstacles may gain longitudinal velocity and obstacle's turbulent eddy shear layers may cause lateral transport.
- **Debris damming on obstacles:** Debris-fields jamming between them should be seen in some cases. Hydrodynamic loads should grow with the dammed surface area.
- **Debris spread:** Across a thinning, slowing inundation wave.
- **Debris come to rest:** Or nearly so, at appropriate distances.
- **Inundation begins to drawdown:** Debris mobilize in reverse for brief drawdown spreading if they are unprotected by obstacles.
- **Debris return to rest:** Wave drawdown flow becomes too weak for continued debris mobilization against friction.

Motion is visualized per debris with respect to their initial spatial configuration, segmented by the experimental case, and with obstacles shown. Upstream (obstacle configurations of 0x0, 5x1, and 5x2) and downstream (0x0 and 5x2) cases with six-debris each (Goseberg et al. 2016b) is illustrated in Figures 11, 12, and 13 for SPH, MPM, and STAR-CCM+ CFD results, respectively.

For SPH in Figure 11, strong characterization of debris motion in both the inundation run up and

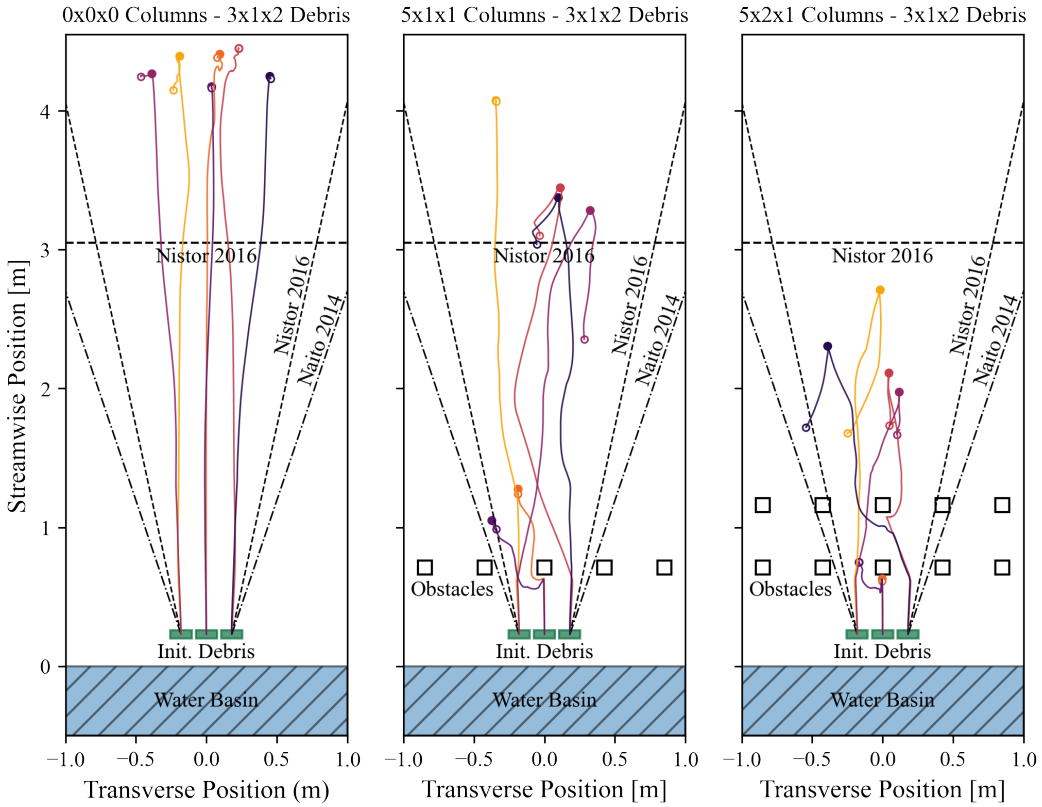

Fig. 11. Debris motion simulated by SPH for Waseda University's tsunami wave basin, viewed top-down. SPH motion-paths of experiments on six debris (two vertical layers of three debris) with zero, one, and two rows of five obstacles present from experiments by Goseberg et al. 2016b. Full circles denote the debris' run up position, while rest positions after drawdown are marked with empty circles. Fitted equations from Naito et al. 2014 and Nistor et al. 2017a give general bounds on anticipated debris motion, with obstacle configurations are seen to influence. A tendency for debris to spread convexly is noted. Simulated by Felix Spröer, Clemens Krautwald, and Nils Goseberg.

drawdown are visible. Qualitatively realistic motion of debris occurs, especially as debris pass each other laterally and cross obstacle eddies. All debris are mobilized, vertical stacks decouple at appropriate times, all debris reach rest or near rest as the run up tapers, debris in the path of drawdown re-mobilize, and said debris attain rest again at reasonable locations in terms of lateral and longitudinal displacement. This is, broadly speaking, an excellent characterization of the motion phases we aim to see. However, there is a noted tendency for debris to glide 20% beyond experimental medians and exceed the experimental envelope for the no obstacle case in Figure 6. In the upstream debris with a single row of obstacles case in Figures 6 and 10, it is shown that 2/6 debris and 1/6 debris are outliers compared to experimental envelopes for longitudinal displacement and lateral spread, respectively. Flow momentum flux that is greater than in the physical experiment, or frictional coefficients that are too low, may be the culprit.

Overall, SPH as implemented in Section 4.2 appears to be a strong contender for both longitudinal and lateral debris motion in this scaled wave flume facilities, lending confidence to its applications at the prototype tsunami scale. Further, the primary influence of the obstacle configurations as observed in Goseberg et al. 2016b are replicated by SPH results, so its use for complex debris motion in port settings with non-collapsed buildings may be appropriate.

For MPM in Figure 12, excellent characterization of run up motion of debris in the initial inundation, as well as the drawdown from the reflecting flow are visible. Lateral motion is decent with some limitations, notably in the observed tendency for "concave" spreading as opposed to the "convex" spread of SPH

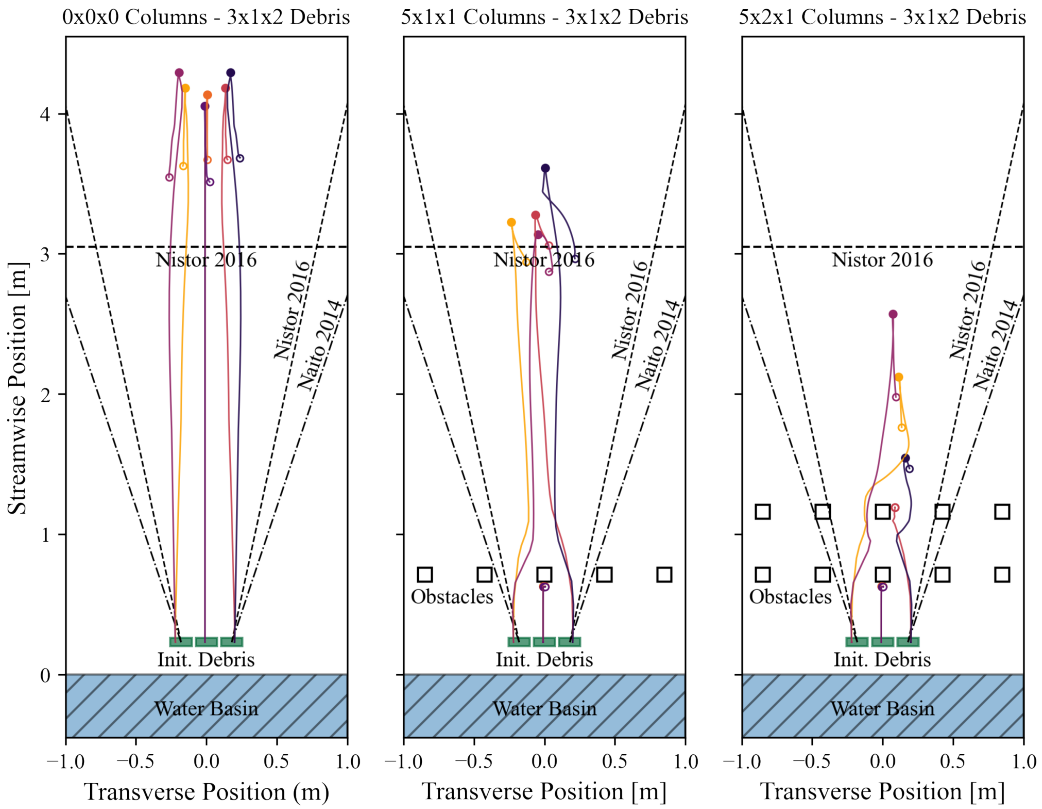

Fig. 12. Debris motion simulated by MPM for Waseda University's tsunami wave basin, viewed top-down. MPM motion-paths of experiments on six debris (two vertical layers of three debris) with zero, one, and two rows of five obstacles present from experiments by Goseberg et al. 2016b. Full circles denote the debris' run up position, while rest positions after drawdown are marked with empty circles. Fitted equations from Naito et al. 2014 and Nistor et al. 2017a give general bounds on anticipated debris motion, with obstacle configurations are seen to influence. A tendency for debris to spread concavely is noted. Simulated by Justin Bonus, Pedro Arduino, and Mike Motley.

results in Figure 11 and experiments by Goseberg et al. 2016b. Besides this finding, qualitatively realistic motion of debris occurs, especially in the ability of debris to interact with each other and columns during transit. Damming can be seen on the central columns in both the single and double row of obstacles cases in Figure 12. However, it is too strong as centerline debris do not move past this column at all, even when adding in 0.01 m of asymmetry. In the double rows of obstacles case, we do not see lateral transport of debris between rows, suggesting that the laminar fluid model impedes motion across obstacle eddies. Overall, MPM produces good characterization of the motion phases we aim to see, with some limitations.

MPM and SPH have a few key differences. MPM debris do not spread out from the centerline as strongly as SPH. This is likely due to lack of turbulence, which alters pressure drag on obstacles and thereby pulling debris into their wakes, but not transporting them across the shear layer. MPM has arguably the strongest results when displacing debris longitudinally, with distances more accurate relative to experiments than even SPH which slightly over-predicts the magnitude; however, small differences in friction coefficients and flow-depths may explain the discrepancies. We also note that MPM debris dam more easily and for longer on obstacles than seen in experiments. This is potentially due to the laminar fluid model or the grid-size dependent contact between debris and fluids.

STAR-CCM+ CFD shows straighter debris transport profiles, with lateral motion being underestimated, as previously discussed on the basis of Figures 10 and 6. The overall motion appears realistic, with

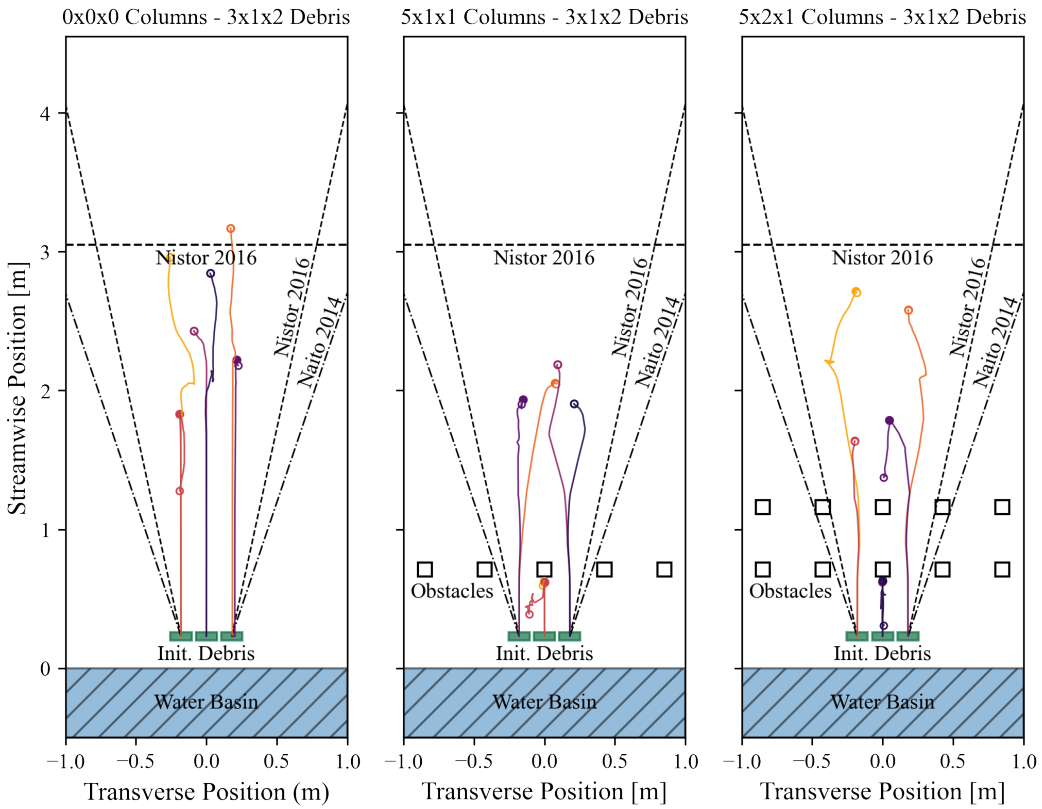

Fig. 13. Debris motion simulated by STAR-CCM+ CFD for Waseda University's tsunami wave basin, viewed top-down. STAR-CCM+ CFD motion-paths of experiments on six debris (two vertical layers of three debris) with zero, one, and two rows of five obstacles present from experiments by Goseberg et al. 2016b. Full circles denote the debris' run up position, while rest positions after drawdown are marked with empty circles. Fitted equations from Naito et al. 2014 and Nistor et al. 2017a give general bounds on anticipated debris motion, which obstacle configurations are seen to influence. Tendency for debris to spread in neither a strongly convex nor concave fashion is noted. Simulated by Andrew Winter.

some limitations. For the non-obstructed harbor apron in Figure 13, the results show a high variety in longitudinal displacements as debris deposited across a large swath of the harbor as the run up inundation thinned with increasing distance from the quay wall. This is unlike results in SPH and MPM, where the flow-depth remained deep enough (relative to debris draft) while crossing the full harbor length to enable transport of the debris group with minimal separation. In other STAR-CCM+ cases, small, abrupt oscillations can be seen in the motion paths, especially following debris impact with the central column and inundation by the reflected drawdown wave. This may be an artifact of the one-way fluid-debris coupling employed. Augmentation with more advanced two-way coupling schemes, which exist in STAR-CCM+, may be a remedy to spurious oscillations in debris motion. Disregarding the broadly underestimated longitudinally displacement, which derives from the artificially increased debris draft, STAR-CCM+ CFD shows all qualitatively expected debris motion phases. For this reason, it is viewed as a broadly capable approach to tsunami debris motion. However, we recommend use of a more in-depth debris-fluid coupling scheme to accurately model Goseberg et al. 2016b, as accurate representation of debris draft is significant to debris dynamics in thin flows as studied by Goseberg et al. 2016b.

5.5 Debris Impact Loads

Advanced 3D numerical analysis of tsunami debris (e.g., in SPH, MPM, CFD) in port settings is typically applied when structural loading is of importance to operations of facilities (e.g., ferry terminals) or when hazardous materials that may threaten local water resources are present (e.g., chemical

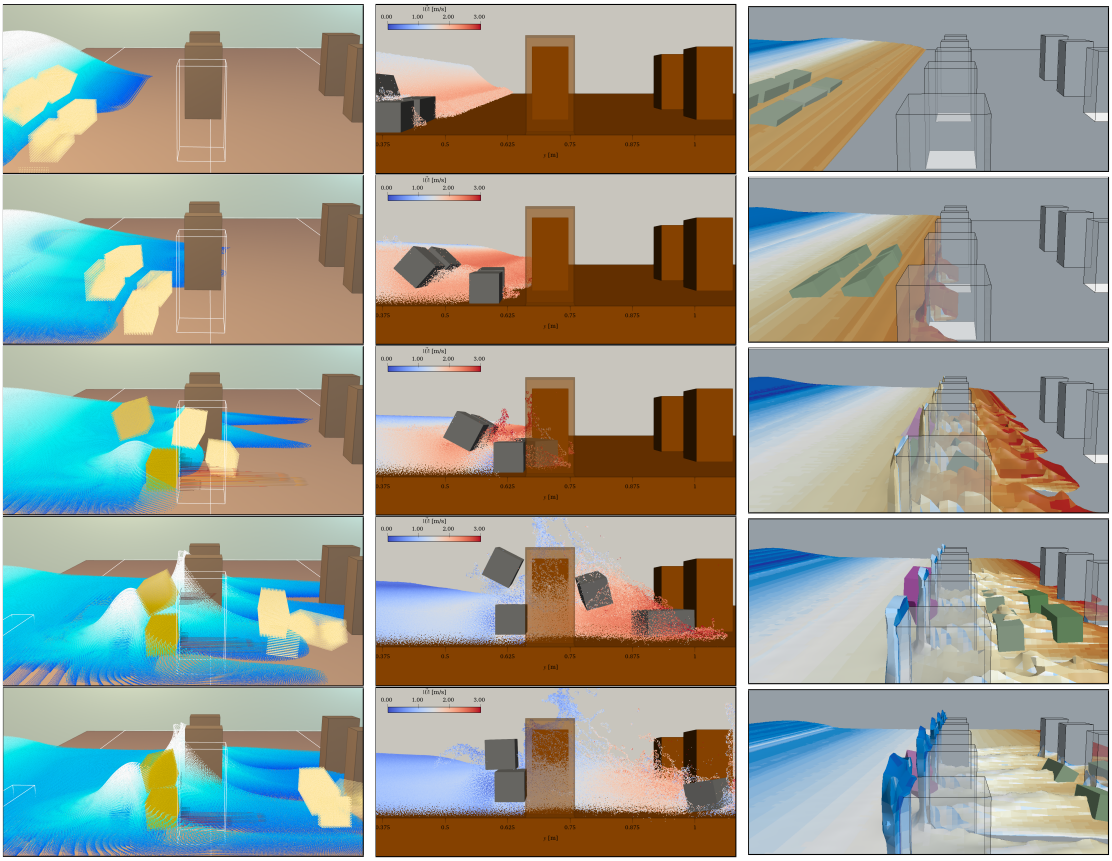

Fig. 14. Debris impact of vertically stacked debris on two rows of obstacles in MPM, SPH, and STAR-CCM+ CFD. (Left) ClaymoreUW MPM, **(Center)** DualSPHysics SPH with Chrono DEM coupling, and **(Right)** STAR-CCM+ CFD with DEM debris. Impact of the stacked debris in the foreground and motion of the background debris compared across methods at key moments.

tanks). Experiments by Goseberg et al. 2016b measured structural loading indirectly by means of debris accelerometer data, sampled at 30 Hz, converted to forces. While the data is low-resolution, it does capture debris impacts as standout events relative to the broader fluid-loading, but the accuracy of magnitudes is questionable and thus matching the experiments is not necessarily good, but a sign that its limitations were replicated. To improve on the experimental readings, debris accelerometers and obstacle load-cells are simulated numerically in the context of analytical guidelines.

Simulation snapshots of debris impacts on obstacles are shown in Figure 14. MPM and SPH exhibit remarkably similar debris motion, but there is a clear difference in the laminar MPM fluid and the turbulent SPH fluid. Larger fluid bulges build behind dammed debris in MPM, as fluid flow around debris is damped proportional to grid-cell size. The impact of both the bottom and top debris (referred to as D3 and D6 in Goseberg et al. 2016b) is near identical in obliquity and elevation in MPM and SPH. However, MPM retrieves this load directly from the obstacles grid-representation, whereas SPH relies on debris particle acceleration data. Of course, SPH can retrieve forces on boundaries as well, though this is exposed to boundary instabilities of the method while MPM can reliably retrieve force from grid-nodes which are used to solve the shared equation of motion for the fluid and debris particles.

Using a basic fluid drag force calculation on a column in the upstream row, we can calculate an expected hydrodynamic force. This will give a more realistic value than the prediction of a full solitary wave impact on a vertical wall as determined in the work of Cross 1967, which is the hydrodynamic upper-bound due to assuming complete wave reflection and also considered herein.

Estimated experimental times of surge arrival at debris and debris impact with the upstream obstacles

are referenced from Goseberg et al. 2016b to ascertain the accuracy of each methods' timescale for debris mobilization to impact.

A collection of aforementioned numerical time-histories, loading equations, and moments of interest are plotted in Figure 15. Plots characterize streamwise load results through either **(i)** an acceleration vector recorded on the debris (i.e., a numerical accelerometer) relative to debris mass or **(ii)** on the shore-oriented face of select column obstacles (i.e., numerical load-cells). SPH and STAR-CCM+ investigate the former to match experimental specifications as closely as possible. MPM used the latter to more precisely characterize the structural demands due to debris impact and damming. SPH and STAR-CCM+ report numerical data from their replication of the debris labeled "D3" from Goseberg et al. 2016b, which corresponds to the bottom-row centerline debris. The MPM results report the far exterior, near exterior, and center columns in the upstream row of obstacles. All methods replicate the experiment case with 5x2 obstacle configuration and six upstream debris.

Arrival time of the wave surge at the debris' initial position from Goseberg et al. 2016b is seen to reasonably match SPH results but is not comparable for MPM as the obstacle load-cells are not yet relevant (i.e., water has reach debris but not the columns). It appears that the lower relative sampling of the accelerometer method in experiments and SPH may reduce the peak debris impact force, but general timing and trends appear similar. Note that the first peak in SPH results is the debris' initial acceleration from rest, while the second and first peak for SPH and MPM results are the debris impact loads, respectively.

The primary finding from loading data in Figure 15 is that MPM performs strongly in prediction of not only hydrodynamic loading on the exterior columns (i.e., columns not directly impacted by debris), matching estimated column drag force values within input variable approximation error, but also in debris impact peaks and subsequent damming loads, both of which exhibit behavior inline with analytical expectations. The MPM debris impact force is closer to an analytical approximation of peak debris impact force, with a percent difference of -45.3%, than SPH and STAR. The analytical approximation for debris impact force relies on a single-degree-of-freedom debris model from Aghl et al. 2014, with an assumed impact velocity of $1.0\,\mathrm{m\,s^{-1}}$, Young's modulus of 0.8 GPa, impact interface width of 0.10 m (assuming full width contact with the square column obstacle), impact interface height of 0.015 m (assuming slight obliquity in impact that reduces interface height to match the interior wall thickness for the top edge of the debris, which contacts the column early due to overtopping from undercutting harbor floor friction), and a density of $921\,\mathrm{kg\,m^{-3}}$. Said assumptions produce a peak force estimate of 407.2 N.

SPH peak force results of 56 N is low compared to analytical assumptions for HDPE plastic debris and alternative numerical methods presented. Even at the lower-bound of estimated impact interface surface area and impact velocity it possesses a percent difference in peak force of -86.0%. However, SPH does recreate the experimental debris accelerometer-style loads with a percent difference of 84.8% which is close than the alternative methods, but this result is inherently limited by the testing apparatus (e.g., use of low-sample rate bluetooth instruments). We emphasize that this does not suggest SPH is a weak candidate for debris load estimation, although it does not prove the contrary either. It is possible that debris loads in SPH may converge towards a magnitude that is more agreeable with existing studies (i.e., relative to impact velocity, effective impact stiffness, debris mass, added mass, and geometric effects, Aghl et al. 2014; Ko et al. 2015; Paczkowski et al. 2012) with higher time resolution and an accurate speed of sound (e.g., as applied in Hasanpour 2023 and Hasanpour et al. 2023). Such adaptations increase computational cost, but will be pursued going forward and with the future advent of more advanced benchmarking datasets.

In lieu of further numerical study with SPH and STAR-CCM+ CFD, we must assume that MPM is the more favorable choice for high-fidelity structural loading in tsunami debris scenarios. Future work will strive to improve SPH and STAR-CCM+ results through more realistic material parameters, high sampling rates, and improved debris-fluid-structure coupling. To aid in subsequent validation efforts, experiment plans must emphasize multi-faceted characterization of debris-structure interactions, e.g., with variable and/or high sampling rate accelerometers and load-cells integrated into every debris and obstacle.

6 SUMMARY AND CONCLUSIONS

In this manuscript, a set of tsunami-debris wave flume experiments performed by Goseberg et al. 2016b

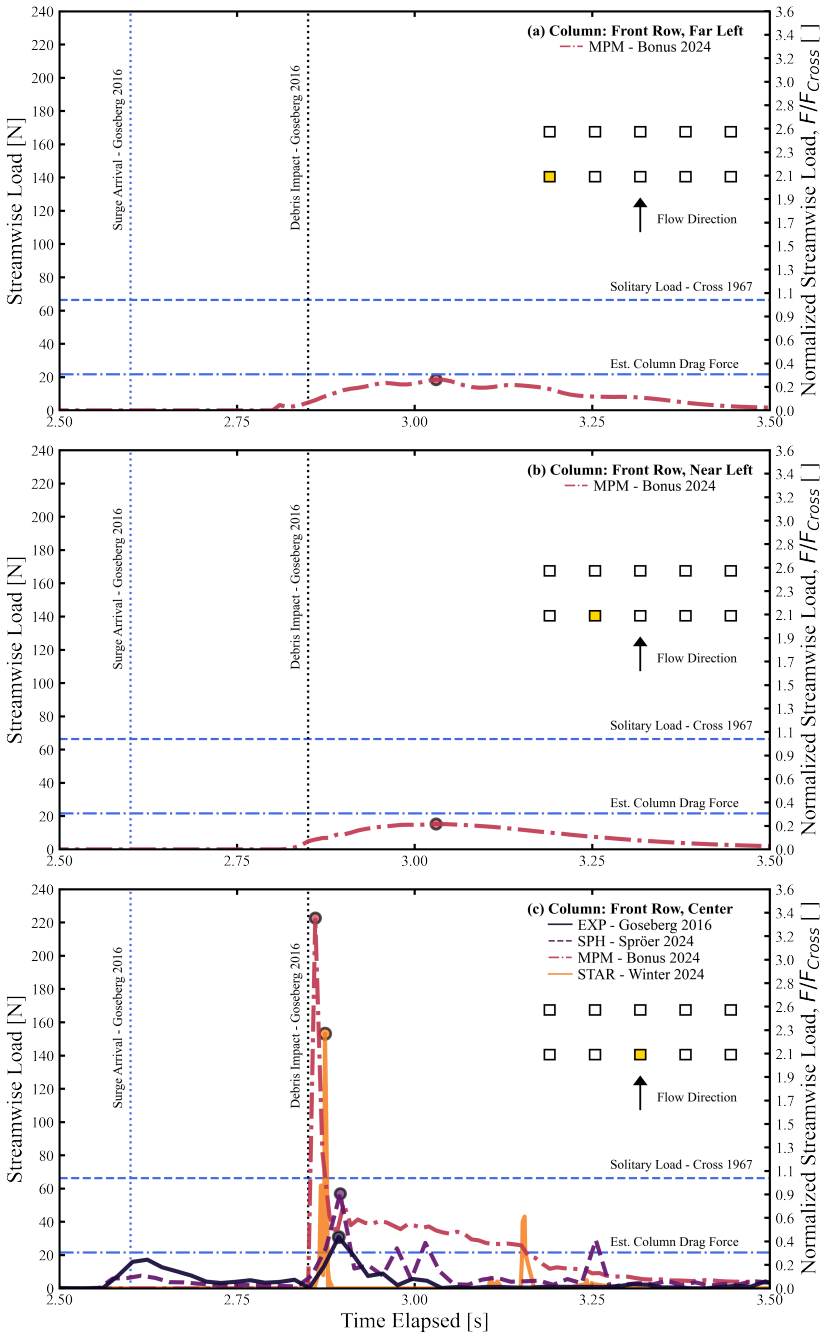

Fig. 15. Wave and debris loads on obstacles. Streamwise loading at three select obstacles in the six debris, two rows of obstacles case of Goseberg et al. 2016b. Loads estimated using numerical load-cells (1200 Hz) on columns in MPM, real / numerical debris accelerometers (30 Hz) in experiments / SPH / STAR-CCM+, and analytical equations for basic fluid drag force around a square column and a full solitary wave reflection load (Cross 1967). (**Top**) MPM measures a hydrodynamic load similar to the drag-force prediction. (**Middle**) MPM measures a hydrodynamic load reduced 10% relative to the far-left column, suggesting a minor positional or debris "shielding" effect. (**Bottom**) MPM measures a max load of 222 N at impact (10x that of columns without impact). Load reduces to a 40 N damming load (2x the drag force estimate, and 0.6x Cross 1967) as debris D3 gets caught on the column before decaying over 0.3 – 0.4 s. SPH captures an 8N mobilization force of debris D3. At impact, SPH debris forces reach 55 N– only 0.25x that of MPM obstacle loads.

Table 3. Qualitative Comparison of Numerical Methods For Simulating Large Debris in Tsunami-Like Waves

	MPM	SPH	STAR-CCM+
Hydrodynamics	★½☆	★★☆	★★½
Debris Longitudinal Spread	★★½	★★☆	★½☆
Debris Lateral Spread	★½☆	★★☆	★★☆
Debris-Obstacle Loads	★★½	★½☆	★★☆

at Waseda University's Tsunami Wave Basin were replicated with and compared between three advanced numerical methods: multi-GPU MPM (ClaymoreUW), GPU SPH (DualSPHysics), and multi-CPU CFD (STAR-CCM+). This comparative endeavor has shed light on the strengths and limitations of these numerical techniques in simulating debris motion in tsunami-like conditions. All three methodologies demonstrated their unique capacities to accurately replicate complex Debris-Fluid-Structure interaction (DFSI) in a controlled, yet highly representative, harbor environment. Table 3 shows a subjective ranking of each numerical method in a set of topics relevant to tsunami-driven debris hazards.

Final benchmark results are summarized for MPM, SPH, and FVM as:

1. For experimental wave gauge free-surface readings of a tsunami-like vacuum-chamber generated wave, total peak magnitude percent differences of [2.4, 1.8, 19.6], [20.8, 2.1, 5.9], [-23.4, -7.9, -18.5], and [-54.5, 47.6, -12.2]% at wave gauges 1, 2, 3, and 4 in [MPM, SPH, STAR].
2. In replication of experimental debris longitudinal displacement, we measured RMSE values of [4.154, 4.650, 6.089] and [3.212, 3.734, 7.260] for runup and drawdown in [MPM, SPH, STAR].
3. In simulation of debris spreading angle, we measured RMSE values of [39.375, 43.439, 40.131] and [42.330, 49.476, 53.019] for runup and drawdown in [MPM, SPH, STAR].
4. For matches to an experimental debris accelerometer-based peak force measurement of 30.8 N and an analytical prediction of 407.2 N, we observe a peak force percent difference of [622.4, 84.8, 396.7] and [-45.3, -86.0, -62.4]% for [MPM, SPH, STAR].

The MPM implementation should be noted to possess:

1. Use of Cauchy's momentum equation with mass conservation to allow for broad capabilities in multi-material, multi-phase, large-deformation dynamics for arbitrarily complex constitutive laws. In composite, it is a unified solution for systems containing fluids, debris, soils, and structures. This is of significant benefit to future studies with the elasto-plastic materials present in prototype tsunami events.
2. The use of a realistic fresh water fluid bulk modulus of 2.0 GPa, corresponding to a speed-of-sound of $1415\,\mathrm{m\,s^{-1}}$.
3. No specific pressure or anti-gravity boundary condition in the flume's fluid reservoir. The water column was allowed to flow out purely due to a gravity measure of $9.806\,65\,\mathrm{m\,s^{-1}}$ s.

The SPH implementation and application has the following notable aspects:

1. Reliance on the Navier-Stokes equations and a coupling to another numerical method to allow for debris dynamics. Although a compressible Navier-Stokes formulations was used, which is more faithful to reality than incompressibility, relying on a coupling technique suggests that SPH itself is limited for tsunami debris studies.
2. The use of a fluid bulk modulus of 3.5 MPa, corresponding to a speed-of-sound of $60\,\mathrm{m\,s^{-1}}$. This is only 0.1 and 4.17% of fresh water's bulk modulus and speed-of-sound at sea-level in normal temperature ranges, which are approximately 2.0 GPa and $1415\,\mathrm{m\,s^{-1}}$. This increased computational speed by approximately 2360%. It also reduces errors common in stiffened systems of equations. Impact dynamics of debris and water at obstacle interfaces may also have been affected, likely reducing total structural loads and affecting readings on numerical debris accelerometers.

3. Application of an empirically tuned anti-gravity boundary condition in the flume's vacuum chamber which assisted in attaining a closer fit to the experimental wave gauge free-surface readings. While a better match in the free-surface may assist in the targeted study of the debris related quantities of interest, it is not faithful to a start-to-finish replication of experiments by Goseberg et al. 2016b. This may bias the produced digital twin to only be appropriate for a small subset of experiments similar to those in Goseberg et al. 2016b.

Use of FVM within STAR-CCM+ as applied by the modeler has the following context:

1. Reliance on the Navier-Stokes equations and a coupling to another numerical method to allow for debris dynamics. An incompressible Navier-Stokes was used, which is not faithful to reality but is extensively applied across engineering fields with some limitations in problems regarding high-frequency impacts, relying on a coupling technique suggests that FVM itself is limited for tsunami debris studies.
2. The use of a fluid bulk modulus of ∞ Pa, corresponding to a speed-of-sound of ∞ m s^{-1} (resulting in infinitely higher bulk modulus and speed-of-sound for fresh water). This increased computational speed as it allows for a different solution approach. It also reduces errors common in stiffened systems of equations. Impact dynamics of debris and water at obstacle interfaces may also have been affected, likely reducing total structural loads and affecting readings on numerical debris accelerometers.
3. Application of complex and physically justified boundary conditions in the flume's vacuum chamber reservoir, including refined pressure valves. This is faithful to a start-to-finish replication of experiments by Goseberg et al. 2016b. Due to uncertainty in the exact release rate of the pressure valves in the physical flume, a parametric study with some educated assumptions had to be undertaken to impose a plausible decay-rate on the vacuum chamber.
4. One-way coupled fluid-debris interaction affects the build-up of dammed fluid masses when debris impact rectangular column obstacles. However, STAR-CCM+ does possess more advanced two-way coupled fluid-debris models which may be pursued in future comparative digital twin studies.

Our findings suggest that while the multi-GPU MPM and GPU SPH perform exceptionally well in capturing the debris longitudinal and lateral spreading, STAR-CCM+ has shown greater precision in estimating wave gauge elevations with first-principals based boundary conditions respective to the pressure release system employed at Waseda University's tsunami wave basin (WU TWB). Both MPM and STAR-CCM+ CFD were observed to measure debris impact loads on square column obstacles with fair magnitude and duration relative to an analytical estimate with baked-in assumptions, while SPH and the experiments themselves sample too coarsely and thus their capability for debris load characterization is inconclusive yet their match is superior. It is important to note, however, that the effectiveness of these methodologies can be scenario-dependent, thus emphasizing the importance of employing a combination of these techniques for comprehensive analysis.

While obstacles were found to have significant influence on the maximum longitudinal displacement of debris, the impact on the spreading angle was found to be less pronounced across all three methods. This study not only offers a critical foundation for further research in optimizing numerical models for tsunami debris motion but also paves the way for the development of more robust, efficient, and reliable disaster management strategies in the face of increasing threats from extreme maritime conditions to ports and coastal communities. As we continue refining and improving these numerical methodologies, it is our hope that they will enable us to better protect coastal communities worldwide.

7 DATA AVAILABILITY STATEMENT

All data, models, or code that support the findings of this study are available from the corresponding author upon reasonable request, e.g. simulations scripts, raw plot data, etc. The full numerical and experimental data-set presented in this manuscript is to be released on the DesignSafe Data-Depot for full public viewing with an estimated date within one month of this articles publishing. Currently, experimental results of Goseberg et al. 2016b alone may be found in a public data-set (Goseberg et al. 2023) at the following host site:

- https://leopard.tu-braunschweig.de/receive/dbbs_mods_00072424

The open-source CPU/GPU accelerated Smoothed Particle Hydrodynamics (SPH) code, DualSPHysics, the Multi-GPU MPM code ClaymoreUW, and the HydroUQ application are available at:

- https://github.com/DualSPHysics/DualSPHysics
- https://github.com/JustinBonus/claymore
- https://github.com/NHERI-SimCenter/HydroUQ

Please note that the ClaymoreUW Multi-GPU MPM software builds on the original Claymore Multi-GPU MPM (Wang et al. 2020), which was developed for primarily graphics purposes and has been retooled and validated by our group for expanded features and engineering usability/accuracy (Bonus 2023). Their open-source code is available at:

- https://github.com/penn-graphics-research/claymore

The Natural Hazard's Engineering Research Institute's (NHERI) open-source application for water-borne hazard uncertainty quantification, HydroUQ (McKenna et al. 2024), features digital twins of the Waseda University's tsunami wave basin (WU TWB) for use in both its built-in ClaymoreUW MPM, with DualSPHysics to be offered in the near-future. HydroUQ's source-code (Windows 8+, Mac OS X, Ubuntu 18.04-LTS) and downloadable release executable files (Windows 8+, Mac OS X) are available at:

- https://github.com/NHERI-SimCenter/HydroUQ
- NHERI-SimCenter/HydroUQ: Version 3.1.0

8 ACKNOWLEDGMENTS

This work was funded in part by the NHERI Computational Modeling and Simulation Center (SimCenter), under NSF awards CMMI 1612843 & 2131111, and in-part by NSF award CMMI 1933184, "Understanding and Quantifying Structural Loading from Tsunami-Induced Debris Fields". Computational resources were provided in-part by the NSF ACCESS program. ACCESS is an advanced computing and data resource program supported by the U.S. National Science Foundation (NSF) under the Office of Advanced Cyberinfrastructure awards No. 2138259 and 2138296.

REFERENCES

Aghl, P. P., Naito, C. J., and Riggs, H. R. (2014). "Full-scale experimental study of impact demands resulting from high mass, low velocity debris." *Journal of Structural Engineering*, 140, 04014006 doi: 10.1061/(ASCE)ST.1943-541X.0000948.

Altomare, C., Scandura, P., Cáceres, I., Viccione, G., et al. (2023). "Large-scale wave breaking over a barred beach: Sph numerical simulation and comparison with experiments." *Coastal Engineering*, 185, 104362.

Anitescu, M. and Tasora, A. (2010). "An iterative approach for cone complementarity problems for non-smooth dynamics." *Computational Optimization and Applications*, 47(2), 207–235.

Ayoub, V., Delenne, C., Chini, M., Finaud-Guyot, P., Mason, D., Matgen, P., Maria-Pelich, R., and Hostache, R. (2022). "A porosity-based flood inundation modelling approach for enabling faster large scale simulations." *Advances in Water Resources*, 162, 104141.

Bihs, H., Chella, M. A., Kamath, A., and Arntsen, A. (2017). "Numerical Investigation of Focused Waves and Their Interaction With a Vertical Cylinder Using REEF3D." *Journal of Offshore Mechanics and Arctic Engineering*, 139(4), 041101.

Bonus, J. (2023). "Evaluation of Fluid-Driven Debris Impacts in a High-Performance Multi-GPU Material Point Method." PhD thesis, University of Washington, Seattle, WA, United States (November).

Bonus, J., Arduino, P., Motley, M., and Eberhard, M. (2022). "Multi-scale numerical simulation of tsunami-driven debris-field impacts." *Proceedings of PORTS '22*, American Society of Civil Engineers, 328–339 (9).

Brackbill, J., Kothe, D., and Zemach, C. (1992). "A continuum method for modeling surface tension." *Journal of Computational Physics*, 100(2), 335–354.

Chen, Z.-P., Zhang, X., Sze, K. Y., Kan, L., and Qiu, X.-M. (2018). "v-p material point method for weakly compressible problems." *Computers Fluids*, 176, 170–181.

Chock, G. Y. (2016). "Design for tsunami loads and effects in the asce 7-16 standard." *J. Struct. Eng*, 142, 4016093.

Cinar, G. E., Keen, A., and Lynett, P. (2022). "Motion of a debris line source under currents and waves: Experimental study." *Journal of Waterway, Port, Coastal and Ocean Engineering*, 149.

Crespo, A. J. C., Gómez-Gesteira, M., and Dalrymple, R. (2007). "Boundary Conditions Generated by Dynamic Particles in SPH Methods." *Computers, Materials & Continua*, 5(3), 173–184.

Cross, R. H. (1967). "Tsunami surge forces." *Journal of the Waterways and Harbors Division*, 93, 201–234.

Dalrymple, R. A. and Rogers, B. D. (2006). "Numerical modeling of water waves with the SPH method." *Coastal Engineering*, 53(2), 141–147.

Derschum, C., Nistor, I., Stolle, J., and Goseberg, N. (2018). "Debris impact under extreme hydrodynamic conditions part 1: Hydrodynamics and impact geometry." *Coastal Engineering*, 141, 24–35.

Domínguez, J. M., Fourtakas, G., Altomare, C., Canelas, R. B., Tafuni, A., García-Feal, O., Martínez-Estévez, I., Mokos, A., Vacondio, R., Crespo, A. J. C., Rogers, B. D., Stansby, P. K., and Gómez-Gesteira, M. (2022). "DualSPHysics: from fluid dynamics to multiphysics problems." *Computational Particle Mechanics*, 9, 867–895.

English, A., Domínguez, J. M., Vacondio, R., Crespo, A. J. C., Stansby, P. K., Lind, S. J., Chiapponi, L., and Gómez-Gesteira, M. (2022). "Modified dynamic boundary conditions (mDBC) for general-purpose smoothed particle hydrodynamics (SPH): Application to tank sloshing, dam break and fish pass problems." *Computational Particle Mechanics*, 9(5), 1–15.

Fei, Y., Huang, L., Guo, Q., Wu, R., and Gao, M. (2021). "Revisiting integration in the material point method: A scheme for easier separation and less dissipation." *ACM Trans. Graph*, 40, 1–16.

Fourtakas, G., Vacondio, R., Dominguez Alonso, J., and Rogers, B. D. (2020). "Improved density diffusion term for long duration wave propagation." 351–357 (January).

Fu, C., Guo, Q., Gast, T., Jiang, C., and Teran, J. (2017). "A polynomial particle-in-cell method." *ACM Transactions on Graphics*, Vol. 36, Association for Computing Machinery (11).

Gautam, D., Adhikari, R., Gautam, S., Pandey, V. P., Thapa, B. R., Lamichhane, S., Talchabhadel, R., Thapa, S., Niraula, S., Aryal, K. R., Lamsal, P., Bastola, S., Sah, S. K., Subedi, S. K., Puri, B., Kandel, B., Sapkota, P., and Rupakhety, R. (2023). "Unzipping flood vulnerability and functionality loss: tale of struggle for existence of riparian buildings." *Natural Hazards*, 119, 989–1009.

Ghodoosipour, B., Stolle, J., Nistor, I., Mohammadian, A., and Goseberg, N. (2019). "Experimental Study on Extreme Hydrodynamic Loading on Pipelines. Part 1: Flow Hydrodynamics." *Journal of Marine Science and Engineering*, 7, 251.

Goseberg, N., Nistor, I., Mikami, T., Shibayama, T., and Stolle, J. (2016a). "Nonintrusive spatiotemporal smart debris tracking in turbulent flows with application to debris-laden tsunami inundation." *Journal of Hydraulic Engineering*, 142(12).

Goseberg, N., Stolle, J., Nistor, I., and Shibayama, T. (2016b). "Experimental analysis of debris motion due the obstruction from fixed obstacles in tsunami-like flow conditions." *Coastal Engineering*, 118, 35–49.

Goseberg, N., Stolle, J., Nistor, I., Shibayama, T., Spröer, F., Krautwald, C., and Goseberg, N. (2023). "Experimental dataset describing the debris motion due to the obstruction from fixed obstacles in tsunami-like flow conditions, <https://leopard.tu-braunschweig.de/receive/dbbs_mods_00072424>.

Goseberg, N., Wurpts, A., and Schlurmann, T. (2013). "Laboratory-scale generation of tsunami and long waves." *Coastal Engineering*, 79, 57–74.

Hasanpour, A. (2023). "Numerical investigation of tsunami-borne debris interaction with coastal bridges." PhD thesis, University of Nevada, Reno, Nevada, United States (5).

Hasanpour, A., Istrati, D., and Buckle, I. (2021). "Coupled SPH–FEM modeling of tsunami-borne large debris flow and impact on coastal structures." *Journal of Marine Science and Engineering*, 9, 1068.

Hasanpour, A., Istrati, D., and Buckle, I. (2023). "Three-dimensional numerical investigation of floating debris effects on bridge superstructures during tsunamis." *Ocean Engineering*, 289, 116262.

Hirt, C. and Nichols, B. (1981). "Volume of Fluid (VOF) Method for the Dynamics of Free Boundaries." *Journal of Computational Physics*, 39(1), 201–225.

Hokugo, A., Nishino, T., and Inada, T. (2011). "Damage and effects caused by tsunami fires: Fire spread, fire fighting and evacuation." *Fire Science and Technology*, 30(4), 117–137.

Hu, Y., Csail, M., Fang, Y. U., Ge, Z., Zhu, Y., Fang, Y., Qu, Z., Prad-Hana, A., and Jiang, C. (2018). "A moving least squares material point method with displacement discontinuity and two-way rigid body coupling method with displacement discontinuity and two-way rigid body coupling." *ACM Trans. Graph*, 37, 146.

Iafrati, A. (2011). "Energy dissipation mechanisms in wave breaking processes: Spilling and highly aerated plunging breaking events." *Journal of Geophysical Research: Oceans*, 116(C7).

Imai, K., Hashimoto, T., Mitobe, Y., Masuta, T., Takahashi, N., and Obayashi, R. (2022). "Development of a practical evaluation method for tsunami debris and its accumulation." *Applied Sciences*, 12(2).

Ishiki, K., Cunningham, L. S., and Rogers, B. D. (2023). "Existing design approaches to nuclear power plants subject to tsunamis: A critical review." *Structures*, 57, 105109.

Issa, R., Violeau, D., Lee, E.-S., and Flament, H. (2010). *Modelling nonlinear water waves with RANS and LES SPH models*. World Scientific, 497–537.

Jiang, C., Schroeder, C., Selle, A., Teran, J., and Stomakhin, A. (2015). "The affine particle-in-cell method." *ACM Transactions on Graphics*, Vol. 34, Association for Computing Machinery, 1–10 (7).

Jiang, C., Schroeder, C., Teran, J., Stomakhin, A., and Selle, A. (2016). "The material point method for simulating continuum materials." *SIGGRAPH 2016 Courses*, Association for Computing Machinery.

Johnson, K. L. (1985). *Contact Mechanics*. Cambridge University Press, Cambridge.

R. W. Johnson, ed. (2016). *Handbook of Fluid Dynamics*. CRC Press, 2^{nd} edition.

Kennedy, A., Barra, J. M., Blunk, A. V., Lynett, P., Keen, A., and Lomonaco, P. (2021). "Array and debris loading, <https://www.designsafe-ci.org/data/browser/public/designsafe.storage.published/PRJ-3157/details-4082949221061881365-242ac117-0001-012>.

Ko, H. T.-S., Cox, D. T., Riggs, H. R., and Naito, C. J. (2015). "Hydraulic experiments on impact forces from tsunami-driven debris." *Journal of Waterway, Port, Coastal, and Ocean Engineering*, 141, 04014043.

Krautwald, C., von Häfen, H., Niebuhr, P., Vögele, K., Stolle, J., Schimmels, S., Schürenkamp, D., Sieder, M., and Goseberg, N. (2022). "Collapse processes and associated loading of square light-frame timber structures due to bore-type waves." *Coastal Engineering*, 177, 104178.

Kumar, K., Salmond, J., Kularathna, S., Wilkes, C., Tjung, E., Biscontin, G., and Soga, K. (2019). "Scalable and modular material point method for large-scale simulations, <https://arxiv.org/abs/1909.13380>.

Leimkuhler, B. and Matthews, C. (2015). *Molecular Dynamics: With Deterministic and Stochastic Numerical Methods*, Vol. 39 of *Interdisciplinary Applied Mathematics*. Springer International Publishing, Cham.

Lind, S. J., Xu, R., Stansby, P. K., and Rogers, B. D. (2012). "Incompressible smoothed particle hydrodynamics for free-surface flows: A generalised diffusion-based algorithm for stability and validations for impulsive flows and propagating waves." *Journal of Computational Physics*, 231(4), 1499–1523.

Ma, S., Zhang, X., and Qiu, X. M. (2009). "Comparison study of mpm and sph in modeling hypervelocity impact problems." *International Journal of Impact Engineering*, 36, 272–282.

Madsen, P. A., Fuhrman, D. R., and Schäffer, H. A. (2008). "On the solitary wave paradigm for tsunamis." *Journal of Geophysical Research: Oceans*, 113.

Majtan, E., Cunningham, L. S., and Rogers, B. D. (2022). "Experimental and numerical investigation of floating large woody debris impact on a masonry arch bridge." *Journal of Marine Science and Engineering*, 10.

Martínez-Estévez, I., Domínguez, J. M., Tagliafierro, B., Canelas, R. B., García-Feal, O., Crespo, A. J. C., and Gómez-Gesteira, M. (2023). "Coupling of an SPH-based solver with a multiphysics library." *Computer Physics Communications*, 283, 108581.

Martínez-Estévez, I., Domínguez, J., Tagliafierro, B., Canelas, R., García-Feal, O., Crespo, A., and Gómez-Gesteira, M. (2023). "Coupling of an sph-based solver with a multiphysics library." *Computer Physics Communications*, 283, 108581.

Mascarenas, D. (2022). "Experimental evaluation of loads from inundation-driven debris fields." Masters thesis, University of Washington, Seattle, WA.

Mast, C. M. (2013). "Modeling landslide-induced flow interactions with structures using the material

point method." PhD thesis, University of Washington, Seattle, WA.
McKenna, F., Bonus, J., Harish, A., and Lewis, N. (2024). "Hydrouq, <https://zenodo.org/records/10902090> (4). NHERI-SimCenter/HydroUQ: Version 3.1.0 (v3.1.0). Zenodo.
Menter, F. (1993). *Zonal Two Equation k-ω Turbulence Models For Aerodynamic Flows*.
Merrifield, M., Firing, Y., Aarup, T., Agricole, W., Brundrit, G., Chang-Seng, D., Farre, R., Kilonsky, B., Knight, W., Kong, L., et al. (2005). "Tide gauge observations of the indian ocean tsunami, december 26, 2004." *Geophysical Research Letters*, 32(9).
Mitsui, J., Altomare, C., Crespo, A. J. C., Domínguez, J. M., Martínez-Estévez, I., Suzuki, T., Kubota, S.-i., and Gómez-Gesteira, M. (2023). "DualSPHysics modelling to analyse the response of Tetrapods against solitary wave." *Coastal Engineering*, 183, 104315.
Monaghan, J. J. (1994). "Simulating free surface flows with sph." *Journal of Computational Physics*, 110, 399–406.
Monaghan, J. J. and Kos, A. (1999). "Solitary Waves on a Cretan Beach." *Journal of Waterway, Port, Coastal, and Ocean Engineering*, 125(3), 145–155.
Moon, W. C., Puay, H. T., and Lau, T. L. (2020). "Robust and efficient 3-d numerical model for the hydrodynamic simulation of tsunami wave on land." *Advances in Water Resources*, 146, 103762.
Moris, J. P., Burke, O., Kennedy, A. B., and Westerink, J. J. (2023). "Wave–current impulsive debris loading on a coastal building array." *Journal of Waterway, Port, Coastal, and Ocean Engineering*, 149, 04022025 doi: 10.1061/(ASCE)WW.1943-5460.0000731.
Murnaghan, F. D. (1944). "The compressibility of media under extreme pressures." *Proceedings of the National Academy of Sciences*, 30, 244–247.
Naito, C., Cercone, C., Riggs, H. R., and Cox, D. (2014). "Procedure for site assessment of the potential for tsunami debris impact." *Journal of Waterway, Port, Coastal, and Ocean Engineering*, 140, 223–232.
Nguyen, V. P., de Vaucorbeil, A., and Bordas, S. (2023). *Karamelo: A Multi-CPU/GPU C++ Parallel MPM Code*. Springer International Publishing, 205–225.
Nistor, I., Goseberg, N., and Stolle, J. (2017a). "Tsunami-driven debris motion and loads: A critical review." *Frontiers in Built Environment*, 3, 2.
Nistor, I., Goseberg, N., Stolle, J., Mikami, T., Shibayama, T., Nakamura, R., and Matsuba, S. (2017b). "Experimental investigations of debris dynamics over a horizontal plane." *Journal of Waterway, Port, Coastal, and Ocean Engineering*, 143, 04016022 doi: 10.1061/(ASCE)WW.1943-5460.0000371.
Paczkowski, K., Riggs, H. R., Naito, C., and Lehmann, A. (2012). "A one-dimensional model for impact forces resulting from high mass, low velocity debris." *Structural Engineering and Structural Mechanics*, 42, 831–847.
Park, H., Koh, M.-J., Cox, D. T., Alam, M. S., and Shin, S. (2021). "Experimental study of debris transport driven by a tsunami-like wave: Application for non-uniform density groups and obstacles." *Coastal Engineering*, 166, 103867.
Pradhana, A., Teran, J., Tampubolon, A. P., Gast, T., Klár, G., Fu, C., Jiang, C., and Museth, K. (2017). "Multi-species simulation of porous sand and water mixtures." *ACM Trans. Graph*, 36.
Qiao, Z., Li, T., Simoni, A., Gregoretti, C., Bernard, M., Wu, S., Shen, W., and Berti, M. (2023). "Numerical modelling of an alpine debris flow by considering bed entrainment." *Frontiers in Earth Science*, 10.
Rumsey, C. L., Pettersson Reif, B. A., and Gatski, T. B. (2006). "Arbitrary steady-state solutions with the k-epsilon model." *AIAA Journal*, 44(7), 1586–1592.
She, Z.-S. and Leveque, E. (1994). "Universal scaling laws in fully developed turbulence." *Phys. Rev. Lett.*, 72, 336–339.
Shekhar, K., Winter, A. O., Alam, M. S., Arduino, P., Miller, G. R., Motley, M. R., Eberhard, M. O., Barbosa, A. R., Lomonaco, P., and Cox, D. T. (2020). "Conceptual evaluation of tsunami debris field damming and impact forces." *Journal of Waterway, Port, Coastal, and Ocean Engineering*, 146, 04020039.
Siemens Digital Industries Software (2023b). "Simcenter STAR-CCM+ User Guide, version 2310." *Theory > Multiphase—Eulerian Approach > Volume of Fluid Method > Surface Tension*, Siemens.
Siemens Digital Industries Software (2023c). "Simcenter STAR-CCM+ User Guide, version 2310." *Theory > Multiphase—Eulerian Approach > Volume of Fluid Method > Surface Tension*, Siemens.

Siemens Digital Industries Software (2023d). "Simcenter STAR-CCM+ User Guide, version 2310." *Physics Simulation > Multiphase Flow > Discrete Element Method (DEM)*, Siemens.
Siemens Digital Industries Software (2023e). "Simcenter STAR-CCM+ User Guide, version 2310." *Theory > Numerical Flow Solution > Finite Volume Discretization > Segregated Flow Solver*, Siemens.
Siemens Digital Industries Software (2023f). "Simcenter STAR-CCM+ User Guide, version 2310." *Physics Simulation > Multiphase Flow > Volume Of Fluid (VOF) Multiphase > VOF Guidelines*, Siemens.
Siemens Digital Industries Software (Siemens 2023a). "Simcenter STAR-CCM+, version 2310.
Sogut, E., Sogut, D. V., and Farhadzadeh, A. (2019). "Effects of building arrangement on flow and pressure fields generated by a solitary wave interacting with developed coasts." *Advances in Water Resources*, 134, 103450.
Stolle, J., Derschum, C., Goseberg, N., Nistor, I., and Petriu, E. (2018). "Debris impact under extreme hydrodynamic conditions part 2: Impact force responses for non-rigid debris collisions." *Coastal Engineering*, 141, 107–118.
Stolle, J., Nistor, I., and Goseberg, N. (2016). "Optical tracking of floating shipping containers in a high-velocity flow." *Coastal Engineering Journal*, 58, 1650005.
Stolle, J., Nistor, I., Goseberg, N., Mikami, T., and Shibayama, T. (2017a). "Entrainment and transport dynamics of shipping containers in extreme hydrodynamic conditions." *Coastal Engineering Journal*, 59(3).
Stolle, J., Nistor, I., Goseberg, N., and Petriu, E. (2020a). "Development of a probabilistic framework for debris transport and hazard assessment in tsunami-like flow conditions." *Journal of Waterway, Port, Coastal, and Ocean Engineering*, 146(5), 04020026.
Stolle, J., Nistor, I., Goseberg, N., and Petriu, E. (2020b). "Multiple debris impact loads in extreme hydrodynamic conditions." *Journal of Waterway, Port, Coastal and Ocean Engineering*, 146(2).
Stolle, J., Takabatake, T., Mikami, T., Shibayama, T., Goseberg, N., Nistor, I., and Petriu, E. (2017b). "Experimental investigation of debris-induced loading in tsunami-like flood events." *Geosciences (Switzerland)*, 7(3).
Stomakhin, A., Schroeder, C., Chai, L., Teran, J., and Selle, A. (2013). "A material point method for snow simulation." *ACM Trans. Graph.*, 32.
Sulsky, D., Chen, Z., and Schreyer, H. L. (1993). "A particle method for history-dependent materials." *Other Information: PBD: Jun 1993*.
Sulsky, D., Chen, Z., and Schreyer, H. L. (1994). "A particle method for history-dependent materials." *Computer Methods in Applied Mechanics and Engineering*, 118, 179–196.
Sun, Z., Li, H., Gan, Y., Liu, H., Huang, Z., and He, L. (2018). "Material point method and smoothed particle hydrodynamics simulations of fluid flow problems: A comparative study." *Progress in Computational Fluid Dynamics, An International Journal*, 18, 1.
Tait, P. G. (1888). *Report on some of the physical properties of fresh water and of sea water*, Vol. II, Part IV. Physics and Chemistry (5) . Sourced from the 1911 reprint of the "*Report on the scientific results of the voyage of H.M.S. Challenger during the years 1873-76.*", available digitally at https://escholarship.org/uc/item/7cs1q13k#main.
Takabatake, T., Stolle, J., Hiraishi, K., Kihara, N., Nojima, K., Shigihara, Y., Arikawa, T., and Nistor, I. (2021). "Inter-model comparison for tsunami debris simulation." *Journal of Disaster Research*, 16, 1030–1044.
Tasora, A., Serban, R., Mazhar, H., Pazouki, A., Melanz, D., Fleischmann, J., Taylor, M., Sugiyama, H., and Negrut, D. (2016). "Chrono: An open source multi-physics dynamics engine." *High Performance Computing in Science and Engineering*, T. Kozubek, R. Blaheta, J. Šístek, M. Rozložník, and M. Čermák, eds., Springer International Publishing, 19–49.
Tran, Q. A., Grimstad, G., and Amiri, S. A. G. (2022). "MPMICE: A hybrid MPM-CFD model for simulating coupled problems in porous media. Application to earthquake-induced submarine landslides.
Tran, Q.-A., Sørlie, E., Grimstad, G., and Eiksund, G. (2023). "Role of hydraulic conductivity on the mechanism of earthquake induced submarine landslides -a cfd-mpm analysis." *10th European Conference on Numerical Methods in Geotechnical Engineering* (7).
von Häfen, H., Stolle, J., Nistor, I., and Goseberg, N. (2021). "Side-by-side entrainment and displacement of cuboids due to a tsunami-like wave." *Coastal Engineering*, 164, 103819.

Wang, X., Qiu, Y., Slattery, S. R., Fang, Y., Li, M., Zhu, S.-C., Zhu, Y., Tang, M., Manocha, D., and Jiang, C. (2020). "A massively parallel and scalable multi-GPU material point method." *ACM Trans. Graph.*, 39.

Wendland, H. (1995). "Piecewise polynomial, positive definite and compactly supported radial functions of minimal degree." *Advances in Computational Mathematics*, 4(1), 389–396.

Winter, A. (2019). "Effects of flow shielding and channeling on tsunami-induced loading of coastal structures." PhD thesis, University of Washington, Seattle, WA, United States (9).

Yang, W. C., Shekhar, K., Arduino, P., Mackenzie-Helnwein, P., and Miller, G. (2017). "Modeling tsunami induced debris impacts on bridge structures using the material point method." *Procedia Engineering*, 175, 175–181.

Yeh, H., Sato, S., and Tajima, Y. (2013). "The 11 March 2011 East Japan earthquake and tsunami: Tsunami effects on coastal infrastructure and buildings." *Pure and Applied Geophysics*, 170, 1019–1031.

Zhang, W., Wu, Z., Peng, C., li, S., Dong, Y., and Yuan, W.-H. (2023). "Modelling large-scale landslide using a GPU-accelerated 3D MPM with an efficient terrain contact algorithm." *Computers and Geotechnics*, 158, 105411.

Zhao, Y., Jiang, C., and Choo, J. (2023). "Circumventing volumetric locking in explicit material point methods: A simple, efficient, and general approach." *arXiv math.NA* (10). Preprint available at https://doi.org/10.48550/arXiv.2209.02466.

Zheng, X., Pisanò, F., Vardon, P. J., and Hicks, M. A. (2021). "An explicit stabilised material point method for coupled hydromechanical problems in two-phase porous media." *Computers and Geotechnics*, 135, 104112.

Zhu, Y. and Bridson, R. (2005). "Animating sand as a fluid." *ACM SIGGRAPH 2005 Papers*.